Radiogenic chromium isotope evidence for the earliest planetary volcanism and crust formation in the solar system

Ke Zhu (朱柯)[1,4]*, Harry Becker[1], Shi-Jie Li[2], Yan Fan[2,3], Xiao-Ning Liu[4] and Tim Elliott[4]

[1] Freie Universität Berlin, Institut für Geologische Wissenschaften, Malteserstr. 74-100, Berlin 12249, Germany

[2] Center for Lunar and Planetary Sciences, Institute of Geochemistry, Chinese Academy of Sciences, Guiyang 550081 China

[3] Department of Geology, Northwest University, Xi'an 710069, China

[4] Bristol Isotope Group, School of Earth Sciences, University of Bristol, Wills Memorial Building, Queen's Road, Bristol BS8 1RJ, United Kingdom

*corresponding author: ke.zhu@bristol.ac.uk

Accepted for publication in MNRAS Letters on June 1, 2022

Abstract

Erg Chech (EC) 002 is a meteorite with andesitic composition, potentially recording the lava crystallization and crust formation of its parent body. Nucleosynthetic Cr isotope composition ($\varepsilon^{54}Cr = -0.35 \pm 0.06$) for EC 002 suggests a non-carbonaceous region of the solar system, and possibly represents the crustal composition of the brachinite parent body. The ^{53}Mn-to-^{53}Cr decay system shows it crystallized at 4566.6 ± 0.6 Ma, i.e., 0.7 ± 0.6 Ma after solar system formation (only considering the cogenetic matrix fractions with similar $\varepsilon^{54}Cr$ values). This age represents the earliest recorded evidence for planetary melting and volcanism in the solar system, suggesting that the planetary crust formation occurred very early, only within the first few hundred thousand years of solar system history. However, the ^{53}Mn-^{53}Cr age does not overlap with ^{26}Al-^{26}Mg dating results, which might indicate that non-carbonaceous achondrites have lower initial $^{26}Al/^{27}Al$ than the canonical value defined by refractory inclusions in carbonaceous chondrites.

Key words: meteorites, meteors, meteoroids; planets and satellites: formation; planets and satellites: composition; astrochemistry.

1. Introduction

Rocky planets are the only harbor for life form in the solar system, so unravelling their origin and history is fundamental for understanding the habitability of planets other than Earth (Cockell et al., 2016; Lineweaver and Chopra, 2012). For example, mantle-crust differentiation on Earth has set boundary conditions through redox conditions and early degassing processes that liquid water can occur on the surface of Earth. Geochemical studies, mainly elemental and isotopic compositions, on the specimens from these planets provide significant information about differentiation processes and their timing. Sample-return missions represent one way to obtain these specimens from the differentiated planets (e.g., Anand et al., 2020), but at great time and expense. Nonchondrite meteorites (including achondrites) also originate from differentiated asteroids and planets, e.g., from Moon, Mars and Vesta, and the angrite and ureilite parent bodies (Agee et al., 2013; Binzel and Xu, 1993; Bischoff et al., 2014; Marchi et al., 2013; Weiss et al., 2008). Some nonchondritic meteorites have a unique mineralogy and bulk composition, indicative of core, mantle and crustal domains of their parent bodies and thus, these samples record large-scale early planetary differentiation events. For instance, ureilites (Mg-rich, dominated by olivine and pyroxene) and iron meteorites (Fe-Ni metal) are from the mantle and core of asteroids respectively, and record planetary mantle differentiation and core formation (Goldstein et al., 2009; Goodrich et al., 2004). In contrast, shergottite and howardite–eucrite–diogenite (HED) meteorites which are inferred to derive from Mars, 4 Vesta and related bodies, reflect a variety of crustal compositions and processes (Mezger et al., 2013; Mittlefehldt, 2015). In addition to the well-known achondrite groups with numerous members, ungrouped achondrites, e.g., Northwest Africa (NWA) 011 (Yamaguchi et al., 2002), Graves Nunatak (GRA) 06128/06129 (Day et al., 2009), NWA 11119 (Srinivasan et al., 2018), and NWA 7325 (Koefoed et al., 2016) expand the compositional range of achondrites towards chemically more evolved compositions (e.g. higher SiO_2 contents) and thus showcase the diversity of planetary and asteroidal crusts in the solar system. Some achondrites , e.g., NWA 11119 and NWA 7325, yield evidence for their accretion and differentiation within the first ~5 million years after the formation of Ca-Al-rich inclusions (CAIs) (Barrat et al., 2021; Koefoed et al., 2016; Srinivasan et al., 2018; Zhu et al., 2019b). Hence, dating more achondrites is beneficial to map the early history of solar system.

Erg Chech (EC) 002 is a recently (2020) recovered achondrite with andesitic composition which formed by asteroid partial melting and fractional crystallization processes (Barrat et al., 2021). Therefore, its crystallization age should record the eruption age of the magma and the formation of part of its early planetary crust. Barrat et al. (2021) and Fang et al. (2022) employed ^{26}Al-^{26}Mg measurements that suggest that this achondrite crystallized at 4564.97 ± 0.01 Ma (*in-situ* SIMS) or at 4565.43 ± 0.01 Ma (MC-ICP-MS) respectively (i.e., 2.33 ± 0.01 Ma and 1.87 ± 0.01 Ma after solar system formation), if the Al-Mg systematics are anchored to CAIs (Amelin et al., 2010; Connelly et al., 2012; Jacobsen et al., 2008). However, these ^{26}Al-^{26}Mg dates would be

~1.2 Ma older if anchored to the D'Orbigny angrite meteorite (Amelin, 2008a; Brennecka and Wadhwa, 2012; Schiller et al., 2015). These different ^{26}Al-^{26}Mg ages may reflect heterogeneity of initial solar system $^{26}Al/^{27}Al$ (Larsen et al., 2011; Sanborn et al., 2019; Schiller et al., 2015; Wimpenny et al., 2019), at least between the CAI and angrite formation regions. Such an age difference can also be analytical or a function of sample heterogeneity. Although it might be expected that minerals within magmatic samples such as EC 002 are homogeneous, previous studies of the primitive achondrite Tafassasset and mantle-derived samples of the ureilite parent body possess heterogeneous mass-independent Cr isotope compositions (Göpel et al., 2015; Kruttasch et al., 2022; Zhu et al., 2020b). Thus, additional isotopic and age constraints on EC 002 from other decay schemes would be useful.

^{53}Mn-^{53}Cr chronometry can also be used for dating events during the first 20 Ma of the solar system (Birck and Allègre, 1988; Glavin et al., 2004; Göpel et al., 2015; Yamashita et al., 2010; Zhu et al., 2019b; Zhu et al., 2020b). Manganese and Cr are relatively abundant in meteorite samples, e.g., usually more than 1000 ppm in chondrites that are regarded as putative planetary precursors (Kallemeyn and Wasson, 1981), and therefore allow precise measurement of Cr isotopic compositions even in small samples. Particularly in achondrites, the variation of the Mn/Cr ratios between minerals is large enough to ensure high-precision ages. For instance, Cr spinels have very low, pyroxenes intermediate and olivine high Mn/Cr ratios, depending on their chemical compositions (Lugmair and Shukolyukov, 1998). The good concordance between U-Pb, ^{182}Hf-^{182}W and ^{53}Mn-^{53}Cr ages in carbonaceous, non-carbonaceous chondrites and achondrites supports an initially homogeneous distribution of the ^{53}Mn/^{55}Mn ratio in both inner and outer Solar System, as is indicated by Gujba CB chondrules: (Bollard et al., 2015; Yamashita et al., 2010); carbonaceous achondrites (Amelin et al., 2019; Sanborn et al., 2019); angrites (Amelin, 2008a; Brennecka and Wadhwa, 2012; Kleine et al., 2012; Zhu et al., 2019b) and eucrite-like achondrites (Wimpenny et al., 2019).

Additionally, mass-independent variations of ^{54}Cr/^{52}Cr ratios, expressed as ε^{54}Cr (per ten thousand isotope ratio deviation relative to NIST standard), serve as fingerprints for presumed domains from which solar system materials were derived (Trinquier et al. 2007). For example, all known carbonaceous chondrite-like (CC) meteorites show ε^{54}Cr values > 0.3, while the non-carbonaceous chondrite-like (NC) meteorites (or bodies) have ε^{54}Cr value < 0.3 (Qin et al., 2010; Trinquier et al., 2007; Zhu et al., 2021a). Hence, the ε^{54}Cr information provides insights into the accretion location of EC 002 in the context of other solar system objects. Furthermore, ε^{54}Cr data enables testing whether or not different mineral fractions in the sample were isotopically equilibrated at the time of their crystallization. Here, we report high-precision radiogenic and nucleosynthetic Cr isotope data for bulk rock and mineral separates of EC 002, aiming at 1) testing the ε^{54}Cr homogeneity inside this achondrite meteorite, 2) understanding the possible initial location of its parent body in the solar system, and 3) dating the crystallization of this meteorite.

2. Results

EC 002 has a porphyritic texture comprising large orthopyroxene xenocrysts, with anhedral Mg-rich cores (Mg# from 0.79 to 0.86), with euhedral rims of lower Mg# (from 0.57 to 0.73), compositionally similar to a population of smaller phenocrysts (Figure 1 and S1). In the matrix, low-Ca and high-Ca pyroxenes (with Mg# of ~0.44 and ~0.55 respectively), plagioclase and K-rich alkali feldspar, silica minerals and spinel occur, which is consistent to the previous petrological studies (Barrat et al., 2021). Their chemical compositions were determined by electronic microprobe (EMP), and the data are shown in Table S1-S5 and Figure S1-S2.

Sample preparation and analytical methods for Cr isotope analysis are described in the Appendices, and the data are reported in Table 1. Bulk EC 002 shows a $\varepsilon^{54}Cr$ value of −0.35 ± 0.06 (Figures S3 and S4), whereas some separated mineral fractions show $\varepsilon^{54}Cr$ heterogeneity (Figure S3). Two pyroxene fractions, XPX and HPX3, and one spinel, SP2 (the HNO_3 + HF leaching residue from XPX), have different $\varepsilon^{54}Cr$ values ranging from −0.17 ± 0.05 to −0.06 ± 0.09, whereas the other mineral fractions and bulk EC 002 have homogeneous $\varepsilon^{54}Cr$ averaging at −0.33 ± 0.10 (2SD, N = 5). Note that, XPX possesses much higher Mg# (0.86) than bulk EC 002 and other pyroxenes in the matrix (0.43 – 0.58). The bulk EC 002 and different mineral components have variable $^{55}Mn/^{52}Cr$ ratios (from 0.014 to 1.999), and if we only consider the four mineral fractions (LPX, HPX1, HPX2 and SP1) with similar $\varepsilon^{54}Cr$ values (Figure 2, S3), they fall on a well-defined correlation line with a slope of 0.516

± 0.040 (2SE) and Y-axis intercept of −0.054 ± 0.050 (2SE, MSWD = 0.90; Figure 4). If the bulk EC 002 is included on the isochron, the slope is 0.506 ± 0.038 (2SE) and Y-axis intercept of −0.064 ± 0.050 (2SE, MSWD = 4.1).

3. Discussion

3.1 Isotopic disequilibrium in Erg Chech 002 and the origin of ε^{54}Cr heterogeneity

Cosmogenic effects can alter mass-independent Cr isotope compositions (Qin et al., 2010; Shima and Honda, 1966), but this likely is not be the case for the ε^{54}Cr heterogeneity inside EC 002. Fe is the major target element for cosmogenic production of Cr isotopes (Shima and Honda, 1966) and it can be seen that the ε^{54}Cr values for EC 002 components do not correlate with Fe/Cr ratios (Figure S5). Further, EC 002 possesses a relatively low cosmic ray exposure age (CREA) of ~26 Ma (Barrat et al., 2021) and a bulk Fe/Cr ratio of 22. Since bulk angrites have longer CREA (up to 60 Ma) and higher Fe/Cr ratios (up to ~600), yet show homogeneous ε^{54}Cr (Zhu et al., 2019b), the cosmogenic effect on Cr isotope compositions on EC 002 should be less than the analytical uncertainty.

From the BSE images of EC 002 (Figure 1), it is clear that there are xenocrystic pyroxenes likely did not crystallize from the current magma host. In detail, the xenocrystic pyroxenes are rich in Mg and poor in Fe (with Mg# > 70; Table S1), compared to all the pyroxenes phenocrysts (with Mg# < 60; Table S2). These chemical differences can be used to distinguish the xenocrystic and matrix pyroxenes; for example, XPX with Mg# of 0.86 can belong to xenocrystic assemblage. Its leaching residue, which comprises spinel (SP2), shows a higher ε^{54}Cr of −0.06 ± 0.09. We interpret the small ε^{54}Cr difference between XPX and SP2 as reflecting Cr exchange between matrix material and XPX at high temperatures, around 1200 °C (Barrat et al., 2021). Thus, the Cr-rich SP2 may most closely represent the Cr isotope composition of the original orthopyroxene xenocryst-spinel inclusion assemblage. Similarly, HPX3 (with Mg# of 0.53 lower than that of XPX) also shows a higher ε^{54}Cr value (−0.17 ± 0.11) than most of other EC 002 components and bulk, which may be also a mixture of inherited higher ε^{54}Cr from the xenocrysts and lower ε^{54}Cr of surrounding melt, now represented by the matrix. The Δ^{17}O values of EC 002 matrix (−0.14 ± 0.01‰; 2SE, N =3) and xenocrysts (−0.11 ± 0.01‰; 2SE, N =4) are also slightly different (Gattacceca et al., 2021), lending support to the notion of isotopic heterogeneity between mineral phases in the EC002 parent body.

Recently, internal ε^{54}Cr heterogeneities were reported from other achondrites. The mineral separates and leachates from Tafassasset [CR-like primitive achondrite] show ε^{54}Cr variability from 1.48 ± 0.12 to 3.71 ± 0.17 (Göpel et al., 2015). Unlike on the EC 002 parent body, Tafassasset only experienced localized partial melting and the melts did not segregate from the residue (Gardner-Vandy et al., 2012). Nevertheless, the Cr isotopic data on Tafassasset show that magmatic conditions may not necessarily homogenize ε^{54}Cr heterogeneities inherited from nebular precursor materials. Other evidence for ε^{54}Cr heterogeneity in achondrites comes from ureilite analyses. The acid leachates of main-group ureilite show ε^{54}Cr values ranging from ~−1.2 to ~−0.8 (Kruttasch et al., 2022),which is consistent with a previous study of samples from the ureilite parent body which reported ε^{54}Cr heterogeneity with values ranging from −0.68

± 0.09 to −1.06 ± 0.04, interpreted to reflect mantle heterogeneity (Zhu et al., 2020b). The ureilite parent body is believed to have undergone core-mantle-crust differentiation (Barrat et al., 2016; Goodrich et al., 1987; Warren et al., 2006). Because both the bulk ureilites and ureilite leachate fractions show the ε^{54}Cr heterogeneity, these results suggest that planetary magmatic processes may not fully homogenize heterogeneous nucleosynthetic isotope signatures. Note that, both Tafassasset and ureilites belong to the primitive achondrites. According to ε^{54}Cr systematics, EC 002 most closely matches the brachinites, which is also a group of primitive achondrites (Keil, 2014). This will be further discussed in the next section.

Another possible origin for the ε^{54}Cr heterogeneity might be late accretion of material with a chondritic bulk composition. Late accretion of chondritic material (Morbidelli and Wood, 2015), can have a major influence on the siderophile budget e.g., Ni, of planetary mantles. However, bulk EC 002 and all the mineral fractions have very low Ni/Mg ratios (Table 1), relative to chondrites with Ni/Mg (atom) ratios of ~0.04 (Alexander, 2019). Assuming mixing between bulk EC002 and CI chondrite, with ε^{54}Cr (highest among chondrites) and Ni/Mg ratios of 1.50 and 0.045 respectively, achieving the Ni/Mg ratio of XPX (~0.004) requires ~90% bulk EC 002. If XPX was mixing by 90% EC 002 + 10% CI chondrites, however, it cannot account for a ε^{54}Cr = XX rather than the value of −0.17 ± 0.06 in XPX. Hence, chondritic contamination as a cause for ε^{54}Cr heterogeneity in EC 002 appears minor.

The ε^{54}Cr difference between EC 002 xenocrysts (up to ~−0.06) and fine-grained andesitic matrix (< −0.35, represented by bulk EC 002) possibly suggests heterogeneous mantle sources of ε^{54}Cr in the EC 002 parent body. The high-Mg pyroxene xenocrysts may have crystallized as magmatic cumulates in the mantle or lower crust of the EC 002 parent body. Then they might have been captured by the andesitic magma that formed from another source region with different ε^{54}Cr signatures, and both were transported close to the surface of the parent body. Possibly due to the small-size of EC 002 parent body and rapid cooling of the magma, the pyroxene xenocrysts were not fully equilibrated and dissolved only partially, and thus were preserved in EC 002. This situation is also indicated by the ε^{53}Cr difference between SP1 (ε^{53}Cr = −0.06 ± 0.06, from the fine-grained matrix) and SP2 (ε^{53}Cr = −0.13 ± 0.05, leaching residue associated with xenocrysts; Figure 1), which suggest using the Mn-Cr model ages (Anand et al., 2021) that spinel in xenocrysts with lower ε^{53}Cr values formed earlier than the spinel in matrix. In details, chromites have Mn/Cr ratios close to 0, their lower ε^{53}Cr values means less radiogenic ^{53}Cr ingrowth and earlier formation.

3.2 Erg Chech 002 derived from a brachinite-like body from the inner solar system

The ε^{54}Cr values for both bulk and all the mineral components are lower than 0.3 (Table 1) and fall in the range of NC materials (Qin et al., 2010; Trinquier et al., 2007; Zhu et al., 2021a), hence the EC 002 parent body likely accreted in the inner Solar System. The ε^{54}Cr value of bulk EC 002, −0.35 ± 0.06 (Figure S4), is similar to angrites

[−0.42 ± 0.13; (Trinquier et al., 2007; Zhu et al., 2019b)], brachinites [−0.44 ± 0.13; (Williams et al., 2020)] and ordinary chondrites [−0.39 ± 0.09; (Pedersen et al., 2019; Qin et al., 2010; Trinquier et al., 2007; Zhu et al., 2021a)]. Mass-independent O isotope compositions, i.e., $\Delta^{17}O = -0.13 \pm 0.03‰$ [2SD, N = 7; average values of matrix and xenocryst; (Gattacceca et al., 2021)] suggest an affinity of EC 002 closest to brachinites with $\Delta^{17}O$ of $-0.23 \pm 0.14‰$ (Figure S4). However, brachinites have a different chemical composition (Keil, 2014) than EC 002 and are ultramafic primitive achondrites that did not undergo large-scale differentiation and presumably come from relatively deep in their parent body (Keil, 2014). In contrast, EC 002, with andesitic petrography and composition, possibly represents a part of the upper crust of the parent body. If EC 002 and brachinites indeed derive from the same parent body, this would imply a partially melted and differentiated body that retained some little differentiated domains and formed from broadly chondritic materials (Collinet and Grove, 2020; Keil, 2014). Thus, a heterogeneous interior of the EC 002 parent body would be indicated if it is related to the brachinites as $\Delta^{17}O$ and $\varepsilon^{54}Cr$ values similar to brachinites suggest. Brachinites are primitive achondrites (Keil, 2014) in which mass-independent isotope compositions have not been fully homogenized by melting processes (Göpel et al., 2015; Zhu et al., 2020b).

3.3 Age of Erg Chech 002, representing the oldest volcanism and crust formation in the solar system

For accurate Mn-Cr isotopic dating, a requirement is that mineral fractions on the isochron formed from an isotopically homogeneous reservoir regarding initial $^{53}Cr/^{52}Cr$ ratios. Hence, the role of the internal $\varepsilon^{54}Cr$ heterogeneities in EC 002 needs to be assessed. Using EC 002 mineral fractions from the matrix portion with similar $\varepsilon^{54}Cr$ values (−0.32 ± 0.11; 2SD, N = 4) for ^{53}Mn-^{53}Cr dating should avoid problems caused by the xenocryst assemblage with different $\varepsilon^{54}Cr$. These proportions with similar $\varepsilon^{54}Cr$ values should reflect crystallization from a common magma source (Figure S3), at the same time, the linear correlation in the isochron diagram suggests that Mn/Cr was not disturbed. The correlation line of $^{55}Mn/^{52}Cr$ and $\varepsilon^{53}Cr$ values (Figure 2) for the mineral fractions with overlapping $\varepsilon^{54}Cr$ values can be interpreted as a ^{53}Mn-^{53}Cr isochron that records fast, magmatic crystallization of the andesite. The slope of the mineral isochron corresponds to a $^{53}Mn/^{55}Mn$ value of $(5.85 \pm 0.45) \times 10^{-6}$ that can be translated to an absolute age of 4566.6 ± 0.6 Ma, i.e., 0.7 ± 0.6 Ma after CAIs, if this age result is anchored to the initial $^{53}Mn/^{55}Mn$ of $(3.24 \pm 0.04) \times 10^{-6}$ for the fast-cooled D'Orbigny angrite which has a well-defined Pb-Pb age of 4563.37 ± 0.25 Ma that has been corrected for U isotope compositions (Amelin, 2008a; Brennecka and Wadhwa, 2012; Glavin et al., 2004). The age uncertainty reflects propagated uncertainties on the slope of the isochron, the half-life of ^{53}Mn, the U-corrected Pb–Pb age, and the $^{53}Mn/^{55}Mn$ ratio of D'Orbigny. The bulk rock of EC 002 has an $\varepsilon^{54}Cr$ consistent with the mineral compositions that define the isochron (Table 1 and Figure S3), suggesting that the fraction of xenocrysts in the Cr isotope balance must be small and within uncertainties. If we include the bulk EC 002 on the ^{53}Mn-^{53}Cr isochron, the $^{53}Mn/^{55}Mn$ ratio and absolute age change only marginally to (5.74 ± 0.43) × 10^{-6} and 4566.5 ± 0.6 Ma, respectively (with a higher MSWD value of 4.1). These two ages with a difference of only ~0.1 Ma are highly consistent. We mainly discuss the age excluding bulk EC 002 due to a much lower MSWD.

We also calculated the Mn-Cr isotope age of the three components with higher $\varepsilon^{54}Cr$ values (SP2, XPX and HPX3), which results in a slope of 0.538 ± 0.044 (2SE, MSWD = 0.36), a Y-axis intercept of -0.147 ± 0.038 (2SE), a $^{53}Mn/^{55}Mn$ ratio of (6.10 ± 0.50) × 10^{-6}, and an absolute age of 4566.8 ± 0.6 Ma (anchored to D'Orbigny).These two similar ages suggests there is only a very short time gap between crystallization for xenocrysts and matrix melt.

Currently, this ^{53}Mn-^{53}Cr age of 4566.6 ± 0.6 Ma for crystallization for EC 002 represents the oldest record of volcanism in the Solar System. For example, the oldest crust formation of Earth and Moon only dates back to ~4.3-4.4 Ga (Borg et al., 2019; O'Neil and Carlson, 2017), and Mars, Vesta and the angrite and main-group aubrite parent bodies show ages of mantle-crust differentiation at ~4547 Ma (Bouvier et al., 2018), 4564.8 ± 0.6 Ma (Trinquier et al., 2008), 4563.2 ± 0.2 Ma (Zhu et al., 2019b) and 4562.5 ± 1.1 Ma (Zhu et al., 2020a), respectively. The crystallization age of EC 002 also predates all those of the other dated achondrites, such as angrites (Amelin, 2008a, b; Connelly et al., 2008), ureilites (Bischoff et al., 2014; Goodrich et al., 2010), NWA 8704/6693, NWA 11119 (Srinivasan et al., 2018), and NWA 7325 (Koefoed et al., 2016). The result strongly supports the notion that advanced silicate differentiation occurred and evolved planetary crust formed very early in the Solar System, i.e., within the first 1 Ma after CAI formation (4567.3 ± 0.1 Ma, (Amelin et al., 2010; Connelly et al., 2012). The crystallization of andesitic crust must postdate both accretion and core formation on the EC 002 parent body, which is also consistent with evidence for early core formation for some asteroids derived from some iron meteorites (Anand et al., 2021; Kruijer et al., 2014). The age for EC 002 is older than some of the chondrule formation ages (Bollard et al., 2017; Connelly et al., 2012; Zhu et al., 2020a). This observation supports previous suggestions that many chondrites and their components reflect younger nebular processes, postdating the oldest differentiated planetesimals, such as the EC 002 parent body. Thus, chondrules may not necessarily reflect an important ingredient in the accretion history of terrestrial planets (Johansen et al., 2015), although this cannot be excluded for earlier chondrule precursors with older generations (Zhu et al., 2019a). Considering its very old age and the short half-life of 0.7 Ma of ^{26}Al, the heat source for melting of the EC 002 parent body must have been the decay of ^{26}Al. The reason why EC 002 cooled and crystallized so early might have been that its parent body was of a much smaller size than the terrestrial planets, since small bodies cannot retain their heat well. The size of the EC 002 parent body may have been smaller than the size of asteroids like Vesta (with mean radius of 262.7 km; (Russell et al., 2012) and the angrite and aubrite (main-group) parent bodies, which differentiated later, at 2.5 – 5 Ma after CAIs (Amelin, 2008a; Trinquier et al., 2008; Zhu et al., 2019b; Zhu et al., 2021b).

3.4 Inconsistencies between ^{53}Mn-^{53}Cr and ^{26}Al-^{26}Mg ages

EC 002 has been dated by the ^{26}Al-^{26}Mg chronometer, resulting in two resolvably different ages, 4564.97 ± 0.01 Ma (Barrat et al., 2021) and 4565.43 ± 0.01 Ma (Fang et al., 2022) by SIMS and MC-ICP-MS respectively. The ^{53}Mn-^{53}Cr age of EC 002 is ~1.1 Ma or ~1.5 Ma older than these two ages. The age inconsistencies between ^{53}Mn-^{53}Cr and ^{26}Al-^{26}Mg chronometry can in principle be 1) xenocryst material was included in the Al-Mg isochron; 2) different closure temperatures of the two systems; 3) ^{26}Al-^{26}Mg systematics may have been disturbed by terrestrial weathering (Luu et al., 2019; Wimpenny et al., 2019); 4) ^{26}Al heterogeneities in the early Solar System (Larsen et al., 2011; Schiller et al., 2015). Fang et al. (2022) did not report the chemical composition (e.g., Mg#) of the EC 002 mineral fractions used to establish their Al-Mg isochron, so it is difficult to estimate the influence from xenocrysts. It is clear that the xenocrysts are older than the matrix mineral assemblage, which is also supported by the ^{53}Mn-^{53}Cr model age for spinels. Including xenocrysts on the isochron will only increase the Al-Mg isochron age, which contradicts its younger age. EC 002 represents an andesitic volcanic rock, implying that most of the rock underwent rapid cooling and crystallization after eruption. Based on the Fe-Mg exchange in the xenocryst assemblage and other mineralogical evidence (Barrat et al., 2021) estimated that the cooling time scale for EC 002 after eruption might have lasted several decades at most, far less than the ^{53}Mn-^{53}Cr and ^{26}Al-^{26}Mg age uncertainty. Hence, the ^{53}Mn-^{53}Cr system and both ^{26}Al-^{26}Mg systems of SIMS and MC-ICP-MS measurements in EC 002 should have closed essentially at the same time. The inconsistent ^{26}Al-^{26}Mg ages dated by SIMS (Barrat et al., 2021) and MC-ICP-MS (Fang et al., 2022) can be mostly attributed to inaccurate Al/Mg ratio measurements on SIMS due to lack of suitable standards, which may cause matrix effects during measurements (Fukuda et al., 2020). Note that, the D'Orbigny anchored ^{26}Al-^{26}Mg age (4566.6 ± 0.01 Ma; 0.7 ± 0.01 Ma after solar system formation) is consistent with the ^{53}Mn-^{53}Cr age (4566.6 ± 0.6 Ma) in this study, in contrast to the CAI-anchored ^{26}Al-^{26}Mg age (4565.4 ± 0.01 Ma; 1.9 ± 0.01 Ma after solar system formation).

Although EC 002 is a meteorite find, its degree of terrestrial weathering is low (Gattacceca et al., 2021). Plagioclase with high Al/Mg ratios mostly controls the slope of the ^{26}Al-^{26}Mg isochron and could have lost Mg in weathering processes on Earth's surface (Luu et al., 2019; Wimpenny et al., 2019). Since terrestrial weathering should only cause mass-dependent Mg isotope fractionation that does not change the mass-independent $\delta^{26}Mg^*$ values, loss of Mg and increasing the Al/Mg ratios for plagioclase would decrease the slope of the ^{26}Al-^{26}Mg isochron and yield a younger age, which would be consistent with the younger ^{26}Al-^{26}Mg age reported in Fang et al. (2022). On the other hand, one of the time anchors, D' Orbigny angrite is also a meteorite find that experienced terrestrial weathering that might disturb the ^{26}Al-^{26}Mg isotope composition in its plagioclase. Schiller et al. (2015) precisely measured the mass-dependent Mg isotope compositions (δ^{25}Mg data) of mineral fractions in D' Orbigny, and showed that the plagioclase with higher Al/Mg ratios have lighter Mg isotope compositions than the bulk, which is inconsistent with a weathering origin from the observation that terrestrial weathering causes isotopically heavier Mg residues (Teng et al., 2010). Hence, it appears that terrestrial weathering is not likely the cause of the age inconsistencies either.

As we discussed in the introduction, different choices of age anchors for the ^{26}Al-^{26}Mg decay system, CAIs vs. the D'Orbigny angrite, result in different ages with a difference of 1 − 1.5 Ma. The differences can be interpreted as a reflection of different initial ^{26}Al/^{27}Al in the CAI accretion region, closest to the Sun (MacPherson et al., 1988; Sossi et al., 2017) compared to the initial ^{26}Al/^{27}Al in the angrite formation region. In fact, CAIs also show large mass-independent isotopic anomalies for multiple elements, e.g., O, Cr and Ti (Krot et al., 2020; Trinquier et al., 2009), which suggest that they formed in different nebula environments compared to achondrites like angrites and EC 002. In Figure 3 and Table S6, we show U-Pb, ^{53}Mn-^{53}Cr and ^{26}Al-^{26}Mg age comparisons for several achondrites. The data indicates that for all NC-like achondrites (ε^{54}Cr values < 0.3; (Zhu et al., 2021a)), their U-Pb ages and, ^{53}Mn-^{53}Cr and ^{26}Al-^{26}Mg ages anchored to D'Orbigny are consistent. This consistency may indicate that the abundance of initial ^{26}Al/^{27}Al value of NC achondrites at 4567 Ma may have been lower in the non-carbonaceous region relative to the canonical initial solar system value of

$^{26}Al/^{27}Al$ derived from CAIs (Schiller et al., 2015). However, for NWA 6704 which has a CR chondrite-like $\varepsilon^{54}Cr$, its ^{53}Mn-^{53}Cr ages are more consistent if its ^{26}Al-^{26}Mg age is anchored to CAIs, which suggests that the ^{26}Al abundance of the CC bodies in the outer solar system may follow that of CAIs. This conclusion is also consistent with the olivine grains (with Al/Mg ratio close to 0) in carbonaceous chondrites having the canonical initial $\mu^{26}Mg$ (~−35 ppm), indicating that the initial ^{26}Al abundance in CCs at 4567 Ma was similar to that of CAIs (Gregory et al., 2020). Thus, the age difference of ^{26}Al-^{26}Mg ages relative to ^{53}Mn-^{53}Cr ages can be caused by a different initial abundance of ^{26}Al in the inner relative to the outer solar system. We note that the U-Pb age of NWA 2976 overlaps the Al-Mg ages anchored to both CAIs and D'Orbigny. This issue warrants more detailed assessment and discussion, e.g., the U-Pb dating (Krestianinov et al., 2021), however, mineral fractions used for dating should avoid xenocrystic material that may have formed at different times and from different sources.

Data Availability Statements

The data underlying this article are available in Zenodo, at https://doi.org/10.5281/zenodo.6513642.

Acknowledgements

K. Z. acknowledges a postdoctoral fellowship from the Alexander von Humboldt Foundation. S.-J. L. thanks a grant from National Natural Science Foundation of China (No. 42173046). T.E. thanks STFC grant (No. ST/V000888/1). Assistance during data collection from Pauline Sandor, Niklas Kallnik, Vitor Barrote, and Carolyn Taylor is also appreciated. Discussions with Peng Ni helped in the interpretation of the data.

Table 1 ^{53}Mn-^{53}Cr data for bulk and mineral components from Erg Chech 002.

EC 002	Mass (g)	Mn	Cr	Ni	Ti	Ni/Mg	Fe/Cr	Ti/Cr	Mg#	^{55}Mn/^{52}Cr	ε^{53}Cr	2SE	ε^{54}Cr	2SE	N
Bulk	0.0394	3837	4135	4	2596	0.00004	22	0.68	0.49	1.322	**0.55**	0.04	**−0.35**	0.06	15
LPX	0.0131	1482	1047	11	1214	0.00026	33	1.26	0.54	1.999	**0.97**	0.05	**−0.27**	0.09	12
HPX1	0.0013	5862	8169	23	2538	0.00011	16	0.34	0.58	1.014	**0.49**	0.04	**−0.41**	0.10	15
HPX2	0.0044	5659	6205	14	2727	0.00009	20	0.48	0.52	1.279	**0.59**	0.05	**−0.29**	0.08	12
SP1						0.09832	0.4	0.16		0.018	**−0.06**	0.06	**−0.31**	0.10	12
SP2						0.04104	0.4	0.12		0.014	**−0.13**	0.05	**−0.06**	0.09	13
XPX						0.00438	4	0.40	0.86	0.165	**−0.07**	0.05	**−0.17**	0.05	15
HPX3	0.0105	5600	8511	5	2914	0.00003	14	0.37	0.53	1.314	**0.56**	0.04	**−0.17**	0.11	15
NIST 3112											**0.02**	0.03	**0.04**	0.06	18
DTS-1											**0.10**	0.04	**0.15**	0.09	8
Allende-a											**0.09**	0.04	**0.84**	0.14	8
Allende-b1											**0.04**	0.07	**0.80**	0.12	10
Allende-b2											**0.05**	0.05	**0.86**	0.06	9
Allende-b3											**0.07**	0.05	**0.84**	0.11	15
Allende-b4											**0.05**	0.03	**0.81**	0.07	7
Allende-ave.											**0.06**	0.04	**0.83**	0.04	2SD

Abbreviations: LPX: low-Ca pyroxene, HPX: high-Ca pyroxene, XPX: xenocrystic pyroxene, SP: spinel.

Note: Mg#, i.e. [Mg]/([Mg]+[Fe]), and other elemental ratios are atomic ratios, while the elemental concentrations are expressed in µg/g. NIST 3112 was also passed through the Cr column chemistry, as for samples. The uncertainty of ^{55}Mn/^{52}Cr (atomic) ratios (measured by *Neptune* MC-ICP-MS) and the elemental concentrations (measured by *Element XR* ICP-MS) are tested as 1% and 10%, respectively (2σ). DTS-1 and Allende-a are analyses of aliquots from the same dissolutions of Zhu et al. (2021b), while the Allende-b is a dissolution of 47.2 mg powder, ground from a ~5g meteorite chip, to homogenize potential internal Cr isotope heterogeneities and so represent bulk Allende. Mg contents of SP1 and SP2 are very low (the Mg concentration in the measurement solution is close to the blank), so we cannot report valid the Mg# for them.

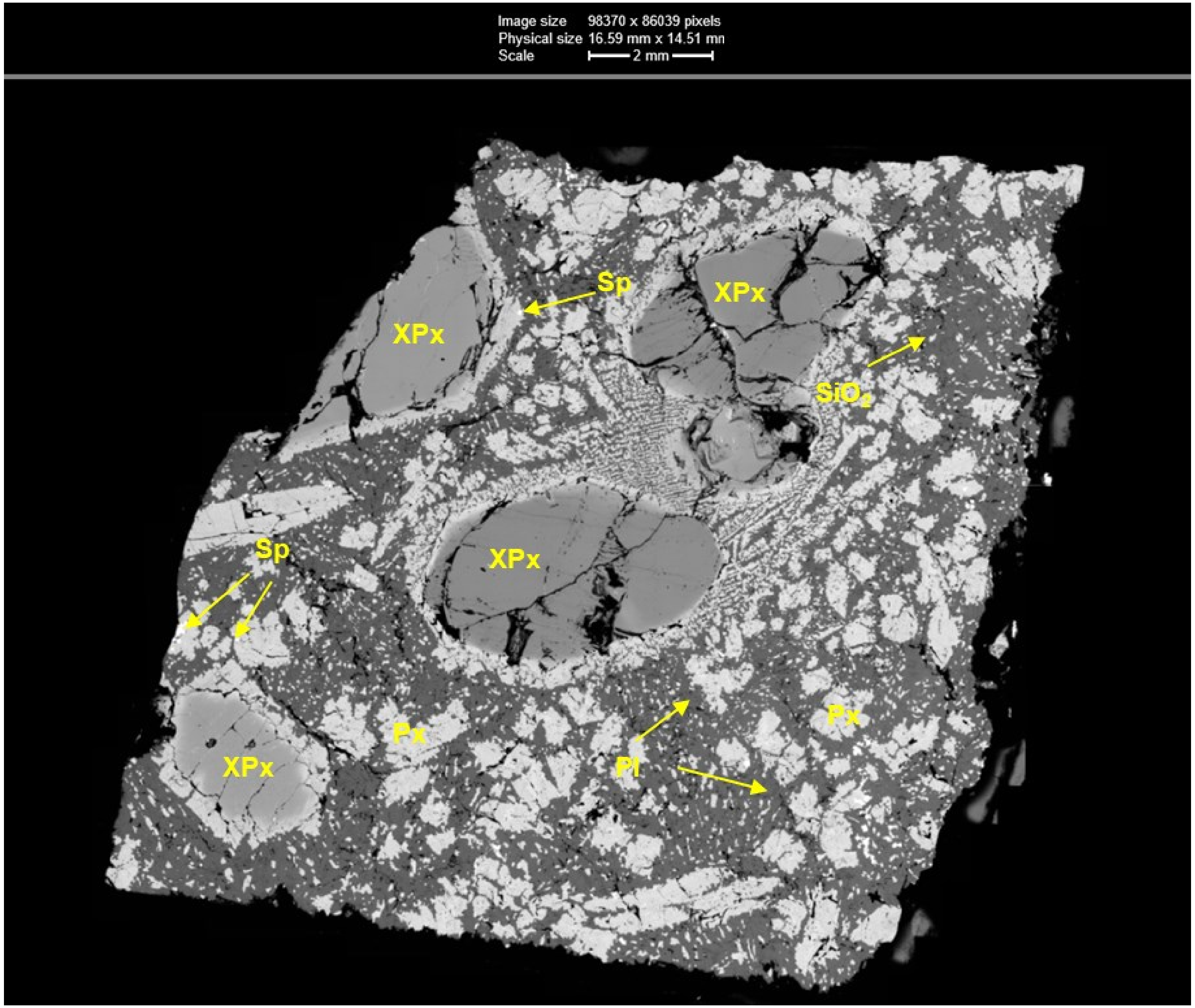

Figure 1 Backscattered Electron for Erg Chech (EC) 002. Mineral abbreviation: XPx, xenocrystic pyroxene; Px, pyroxene; Sp, Spinel; Pl, plagioclase. Note that, the mineral separates for isotope analysis are not related to the minerals in this figure.

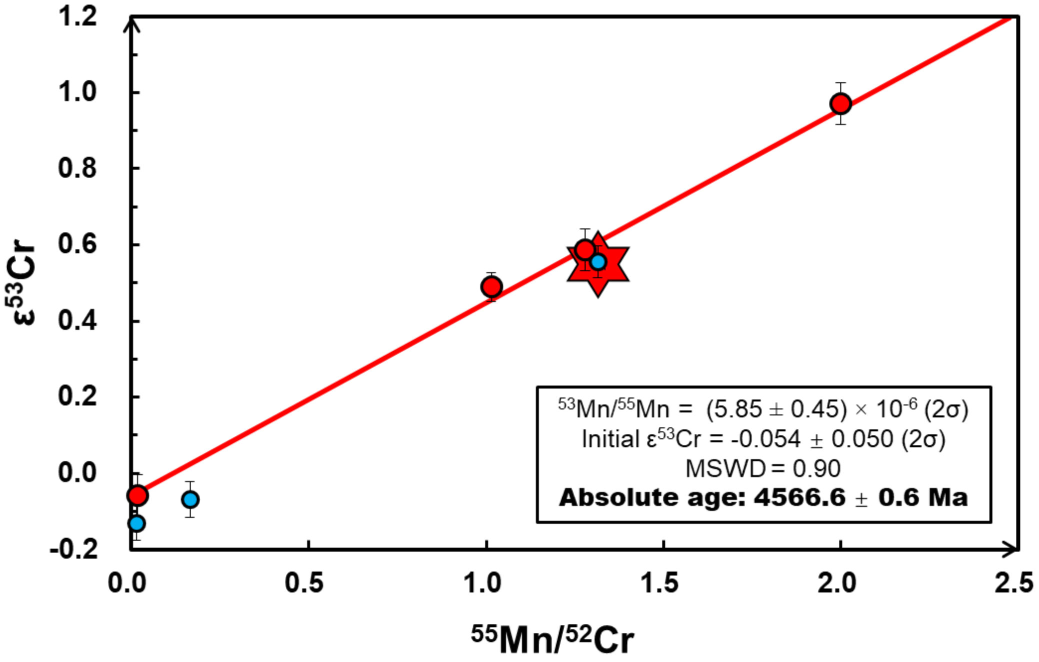

Figure 2 ^{53}Mn-^{53}Cr isochron for Erg Chech (EC) 002. The red star represents bulk EC 002. Red points are the mineral fractions with bulk rock-like ε^{54}Cr values (-0.33 ± 0.10, 2SD), while the blue points possess components with lower ε^{54}Cr values, which are not included in the isochron. The sample of bulk EC 002 is excluded from the fit shown, given its xenocrysts included and effect on the MSWD. If we include it, the ^{53}Mn/^{55}Mn ratio and absolute age slightly changes to (5.74 ± 0.43) × 10^{-6} and 4566.5 ± 0.6 Ma, respectively but the MSWD increases to 4.1. The three components with higher ε^{54}Cr values (blue circles) define a slightly older ^{53}Mn-^{53}Cr age of 4566.8 ± 0.6 Ma (MSWD = 0.36).

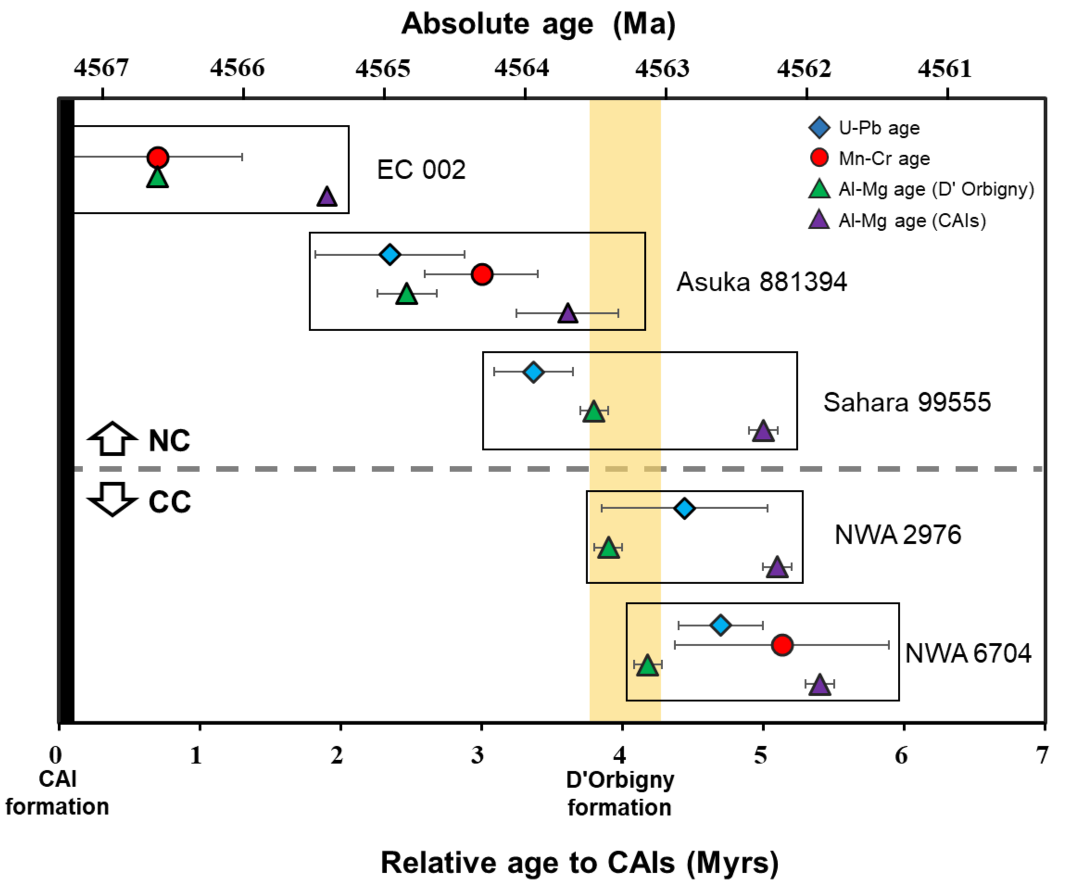

Figure 3 Age comparison for achondrites dated by U-Pb, Mn-Cr and Al-Mg chronometry (with both CAI and D'Orbigny anchors). The detailed data are shown in Table S6. The black and orange bars show the Pb-Pb ages (and uncertainties) for CAIs and D'Orbigny respectively.

References:

Agee, C.B., Wilson, N.V., McCubbin, F.M., Ziegler, K., Polyak, V.J., Sharp, Z.D., Asmerom, Y., Nunn, M.H., Shaheen, R., Thiemens, M.H., 2013. Unique meteorite from early Amazonian Mars: Water-rich basaltic breccia Northwest Africa 7034. Science, 1228858.

Alexander, C.M.O.D., 2019. Quantitative models for the elemental and isotopic fractionations in chondrites: The carbonaceous chondrites. Geochimica et Cosmochimica Acta 254, 277-309.

Amelin, Y., 2008a. U–Pb ages of angrites. Geochimica et Cosmochimica Acta 72, 221-232.

Amelin, Y., 2008b. The U–Pb systematics of angrite Sahara 99555. Geochimica et Cosmochimica Acta 72, 4874-4885.

Amelin, Y., Kaltenbach, A., Iizuka, T., Stirling, C.H., Ireland, T.R., Petaev, M., Jacobsen, S.B., 2010. U–Pb chronology of the Solar System's oldest solids with variable 238U/235U. Earth and Planetary Science Letters 300, 343-350.

Amelin, Y., Koefoed, P., Iizuka, T., Assis Fernandes, V., Huyskens, M.H., Yin, Q.-Z., Irving, A.J., 2019. U-Pb, Rb-Sr and Ar-Ar systematics of the ungrouped achondrites Northwest Africa 6704 and Northwest Africa 6693. Geochimica et Cosmochimica Acta, 628-642.

Anand, A., Pape, J., Wille, M., Mezger, K., Hofmann, B., 2021. Early differentiation of magmatic iron meteorite parent bodies from Mn–Cr chronometry. Geochemical Perspectives Letters 20, 6-10.

Anand, M., Russell, S., Lin, Y., Wadhwa, M., Marhas, K.K., Tachibana, S., 2020. Editorial to the Topical Collection: Role of Sample Return in Addressing Major Questions in Planetary Sciences. Space Science Reviews 216, 101.

Barrat, J.-A., Chaussidon, M., Yamaguchi, A., Beck, P., Villeneuve, J., Byrne, D.J., Broadley, M.W., Marty, B., 2021. A 4,565-My-old andesite from an extinct chondritic protoplanet. Proceedings of the National Academy of Sciences 118, e2026129118.

Barrat, J.-A., Jambon, A., Yamaguchi, A., Bischoff, A., Rouget, M.-L., Liorzou, C., 2016. Partial melting of a C-rich asteroid: Lithophile trace elements in ureilites. Geochimica et Cosmochimica Acta 194, 163-178.

Binzel, R.P., Xu, S., 1993. Chips off of asteroid 4 Vesta: evidence for the parent body of balsaltic achondrite meteorites. Science 260, 186-192.

Birck, J.-L., Allègre, C.J., 1988. Manganese—chromium isotope systematics and the development of the early Solar System. Nature 331, 579-584.

Bischoff, A., Horstmann, M., Barrat, J.-A., Chaussidon, M., Pack, A., Herwartz, D., Ward, D., Vollmer, C., Decker, S., 2014. Trachyandesitic volcanism in the early solar system. Proceedings of the National Academy of Sciences 111, 12689-12692.

Bollard, J., Connelly, J.N., Bizzarro, M., 2015. Pb-Pb dating of individual chondrules from the CBa chondrite Gujba: Assessment of the impact plume formation model. Meteoritics & Planetary Science 50, 1197-1216.

Bollard, J., Connelly, J.N., Whitehouse, M.J., Pringle, E.A., Bonal, L., Jørgensen, J.K., Nordlund, Å., Moynier, F., Bizzarro, M., 2017. Early formation of planetary building blocks inferred from Pb isotopic ages of chondrules. Science Advances 3, e1700407.

Borg, L.E., Gaffney, A.M., Kruijer, T.S., Marks, N.A., Sio, C.K., Wimpenny, J., 2019. Isotopic evidence for a young lunar magma ocean. Earth and Planetary Science Letters 523, 115706.

Bouvier, A., Spivak-Birndorf, L.J., Brennecka, G.A., Wadhwa, M., 2011. New constraints on early Solar System chronology from Al–Mg and U–Pb isotope systematics in the unique basaltic achondrite Northwest Africa 2976. Geochimica et Cosmochimica Acta 75, 5310-5323.

Bouvier, L.C., Costa, M.M., Connelly, J.N., Jensen, N.K., Wielandt, D., Storey, M., Nemchin, A.A., Whitehouse, M.J., Snape, J.F., Bellucci, J.J., 2018. Evidence for extremely rapid magma ocean crystallization and crust formation on Mars. Nature 558, 568-589.

Brennecka, G.A., Wadhwa, M., 2012. Uranium isotope compositions of the basaltic angrite meteorites and the chronological implications for the early Solar System. Proceedings of the National Academy of Sciences 109, 9299-9303.

Cockell, C.S., Bush, T., Bryce, C., Direito, S., Fox-Powell, M., Harrison, J.P., Lammer, H., Landenmark, H., Martin-Torres, J., Nicholson, N., 2016. Habitability: a review. Astrobiology 16, 89-117.

Collinet, M., Grove, T.L., 2020. Formation of primitive achondrites by partial melting of alkali-undepleted planetesimals in the inner solar system. Geochimica et Cosmochimica Acta 277, 358-376.

Connelly, J.N., Bizzarro, M., Krot, A.N., Nordlund, Å., Wielandt, D., Ivanova, M.A., 2012. The absolute chronology and thermal processing of solids in the solar protoplanetary disk. Science 338, 651-655.

Connelly, J.N., Bizzarro, M., Thrane, K., Baker, J.A., 2008. The Pb–Pb age of Angrite SAH99555 revisited. Geochimica et Cosmochimica Acta 72, 4813-4824.

Day, J.M.D., Ash, R.D., Liu, Y., Bellucci, J.J., Rumble Iii, D., McDonough, W.F., Walker, R.J., Taylor, L.A., 2009. Early formation of evolved asteroidal crust. Nature 457, 179-182.

Fang, L., Frossard, P., Boyet, M., Bouvier, A., Barrat, J.-A., Chaussidon, M., Moynier, F., 2022. Half-life and initial Solar System abundance of 146Sm determined from the oldest andesitic meteorite. Proceedings of the National Academy of Sciences 119, e2120933119.

Gardner-Vandy, K.G., Lauretta, D.S., Greenwood, R.C., McCoy, T.J., Killgore, M., Franchi, I.A., 2012. The Tafassasset primitive achondrite: Insights into initial stages of planetary differentiation. Geochimica et Cosmochimica Acta 85, 142-159.

Gattacceca, J., McCubbin, F.M., Grossman, J., Bouvier, A., Bullock, E., Chennaoui Aoudjehane, H., Debaille, V., D'orazio, M., Komatsu, M., Miao, B., 2021. The Meteoritical Bulletin, No. 109. Meteoritics & Planetary Science 56, 1626-1630.

Glavin, D., Kubny, A., Jagoutz, E., Lugmair, G., 2004. Mn-Cr isotope systematics of the D'Orbigny angrite. Meteoritics & Planetary Science 39, 693-700.

Goldstein, J.I., Scott, E.R.D., Chabot, N.L., 2009. Iron meteorites: Crystallization, thermal history, parent bodies, and origin. Geochemistry 69, 293-325.

Goodrich, C.A., Hutcheon, I.D., Kita, N.T., Huss, G.R., Cohen, B.A., Keil, K., 2010. 53Mn–53Cr and 26Al–26Mg ages of a feldspathic lithology in polymict ureilites. Earth and Planetary Science Letters 295, 531-540.

Goodrich, C.A., Jones, J.H., Berkley, J.L., 1987. Origin and evolution of the ureilite parent magmas: Multi-stage igneous activity on a large parent body. Geochimica et Cosmochimica Acta 51, 2255-2273.

Goodrich, C.A., Scott, E.R., Fioretti, A.M., 2004. Ureilitic breccias: clues to the petrologic structure and impact disruption of the ureilite parent asteroid. Chemie der Erde-Geochemistry 64, 283-327.

Göpel, C., Birck, J.-L., Galy, A., Barrat, J.-A., Zanda, B., 2015. Mn–Cr systematics in primitive meteorites: Insights from mineral separation and partial dissolution. Geochimica et Cosmochimica Acta 156, 1-24.

Gregory, T., Luu, T.-H., Coath, C.D., Russell, S.S., Elliott, T., 2020. Primordial formation of major silicates in a protoplanetary disc with homogeneous 26Al/27Al. Science Advances 6, eaay9626.

Jacobsen, B., Yin, Q.-z., Moynier, F., Amelin, Y., Krot, A.N., Nagashima, K., Hutcheon, I.D., Palme, H., 2008. 26 Al–26 Mg and 207 Pb–206 Pb systematics of Allende CAIs: Canonical solar initial 26 Al/27 Al ratio reinstated. Earth and Planetary Science Letters 272, 353-364.

Johansen, A., Low, M.-M.M., Lacerda, P., Bizzarro, M., 2015. Growth of asteroids, planetary embryos, and Kuiper belt objects by chondrule accretion. Science Advances 1, e1500109.

Kallemeyn, G.W., Wasson, J.T., 1981. The compositional classification of chondrites—I. The carbonaceous chondrite groups. Geochimica et Cosmochimica Acta 45, 1217-1230.

Keil, K., 2014. Brachinite meteorites: Partial melt residues from an FeO-rich asteroid. Geochemistry 74, 311-329.

Kleine, T., Hans, U., Irving, A.J., Bourdon, B., 2012. Chronology of the angrite parent body and implications for core formation in protoplanets. Geochimica et Cosmochimica Acta 84, 186-203.

Koefoed, P., Amelin, Y., Yin, Q.-Z., Wimpenny, J., Sanborn, M.E., Iizuka, T., Irving, A.J., 2016. U–Pb and Al–Mg systematics of the ungrouped achondrite Northwest Africa 7325. Geochimica et Cosmochimica Acta 183, 31-45.

Krestianinov, E., Datta, C., Amelin, Y., 2021. Uranium Isotopic Composition of Volcanic Angrites Northwest Africa 12320, Northwest Africa 12004, and Northwest Africa 12774 and Ungrouped Achondrite Erg Chech 002. LPI Contributions 2609, 6059.

Krot, A.N., Nagashima, K., Lyons, J.R., Lee, J.-E., Bizzarro, M., 2020. Oxygen isotopic heterogeneity in the early Solar System inherited from the protosolar molecular cloud. Science advances 6, eaay2724.

Kruijer, T., Touboul, M., Fischer-Gödde, M., Bermingham, K., Walker, R., Kleine, T., 2014. Protracted core formation and rapid accretion of protoplanets. Science 344, 1150-1154.

Kruttasch, P.M., Anand, A., Mezger, K., 2022. Chromium Isotope Systematics of the Chromite-Bearing Ureilites LaPaz Icefield 03587 and Cumulus Hills 04048. LPI Contributions 2678, 2107.

Larsen, K.K., Trinquier, A., Paton, C., Schiller, M., Wielandt, D., Ivanova, M.A., Connelly, J.N., Nordlund, Å., Krot, A.N., Bizzarro, M., 2011. Evidence for magnesium isotope heterogeneity in the solar protoplanetary disk. The Astrophysical Journal Letters 735, L37.

Lineweaver, C.H., Chopra, A., 2012. The Habitability of Our Earth and Other Earths: Astrophysical, Geochemical, Geophysical, and Biological Limits on Planet Habitability. Annual Review of Earth and Planetary Sciences 40, 597-623.

Lugmair, G., Shukolyukov, A., 1998. Early solar system timescales according to 53 Mn-53 Cr systematics. Geochimica et Cosmochimica Acta 62, 2863-2886.

Luu, T.-H., Hin, R.C., Coath, C.D., Elliott, T., 2019. Bulk chondrite variability in mass independent magnesium isotope compositions – Implications for initial solar system 26Al/27Al and the timing of terrestrial accretion. Earth and Planetary Science Letters 522, 166-175.

MacPherson, G.J., Wark, D., Armstrong, J.T., 1988. Primitive material surviving in chondrites-Refractory inclusions. Meteorites and the early solar system 1, 746-807.

Marchi, S., Bottke, W.F., Cohen, B.A., Wünnemann, K., Kring, D.A., McSween, H.Y., De Sanctis, M.C., O'Brien, D.P., Schenk, P., Raymond, C.A., Russell, C.T., 2013. High-velocity collisions from the lunar cataclysm recorded in asteroidal meteorites. Nature Geoscience 6, 303-307.

Mezger, K., Debaille, V., Kleine, T., 2013. Core formation and mantle differentiation on Mars. Space science reviews 174, 27-48.

Mittlefehldt, D.W., 2015. Asteroid (4) Vesta: I. The howardite-eucrite-diogenite (HED) clan of meteorites. Chemie der Erde-Geochemistry 75, 155-183.

Morbidelli, A., Wood, B.J., 2015. Late accretion and the late veneer. The Early Earth: Accretion and Differentiation, Geophysical Monograph 212, 71-82.

O'Neil, J., Carlson, R.W., 2017. Building Archean cratons from Hadean mafic crust. Science 355, 1199-1202.

Pedersen, S.G., Schiller, M., Connelly, J.N., Bizzarro, M., 2019. Testing accretion mechanisms of the H chondrite parent body utilizing nucleosynthetic anomalies. Meteoritics & Planetary Science 54, 1215-1227.

Qin, L., Alexander, C.M.O.D., Carlson, R.W., Horan, M.F., Yokoyama, T., 2010. Contributors to chromium isotope variation of meteorites. Geochimica et Cosmochimica Acta 74, 1122-1145.

Russell, C., Raymond, C., Coradini, A., McSween, H., Zuber, M.T., Nathues, A., De Sanctis, M.C., Jaumann, R., Konopliv, A., Preusker, F., 2012. Dawn at Vesta: Testing the protoplanetary paradigm. Science 336, 684-686.

Sanborn, M.E., Wimpenny, J., Williams, C.D., Yamakawa, A., Amelin, Y., Irving, A.J., Yin, Q.-Z., 2019. Carbonaceous Achondrites Northwest Africa 6704/6693: Milestones for Early Solar System Chronology and Genealogy. Geochimica et Cosmochimica Acta 245, 577-596.

Schiller, M., Baker, J.A., Bizzarro, M., 2010. 26Al–26Mg dating of asteroidal magmatism in the young Solar System. Geochimica et Cosmochimica Acta 74, 4844-4864.

Schiller, M., Connelly, J.N., Glad, A.C., Mikouchi, T., Bizzarro, M., 2015. Early accretion of protoplanets inferred from a reduced inner solar system 26Al inventory. Earth and Planetary Science Letters 420, 45-54.

Shima, M., Honda, M., 1966. Distribution of spallation produced chromium between alloys in iron meteorites. Earth and Planetary Science Letters 1, 65-74.

Sossi, P.A., Moynier, F., Chaussidon, M., Villeneuve, J., Kato, C., Gounelle, M., 2017. Early Solar System irradiation quantified by linked vanadium and beryllium isotope variations in meteorites. Nature Astronomy 1, 0055.

Srinivasan, P., Dunlap, D.R., Agee, C.B., Wadhwa, M., Coleff, D., Ziegler, K., Zeigler, R., McCubbin, F.M., 2018. Silica-rich volcanism in the early solar system dated at 4.565 Ga. Nature Communications 9, 3036.

Teng, F.-Z., Li, W.-Y., Rudnick, R.L., Gardner, L.R., 2010. Contrasting lithium and magnesium isotope fractionation during continental weathering. Earth and Planetary Science Letters 300, 63-71.

Tissot, F.L.H., Dauphas, N., Grove, T.L., 2017. Distinct 238U/235U ratios and REE patterns in plutonic and volcanic angrites: Geochronologic implications and evidence for U isotope fractionation during magmatic processes. Geochimica et Cosmochimica Acta 213, 593-617.

Trinquier, A., Birck, J.-L., Allègre, C.J., 2007. Widespread 54Cr heterogeneity in the inner solar system. The Astrophysical Journal 655, 1179-1185.

Trinquier, A., Birck, J.L., Allègre, C.J., Göpel, C., Ulfbeck, D., 2008. 53Mn–53Cr systematics of the early Solar System revisited. Geochimica et Cosmochimica Acta 72, 5146-5163.

Trinquier, A., Elliott, T., Ulfbeck, D., Coath, C., Krot, A.N., Bizzarro, M., 2009. Origin of Nucleosynthetic Isotope Heterogeneity in the Solar Protoplanetary Disk. Science 324, 374-376.

Wadhwa, M., Amelin, Y., Bogdanovski, O., Shukolyukov, A., Lugmair, G.W., Janney, P., 2009. Ancient relative and absolute ages for a basaltic meteorite: Implications for

timescales of planetesimal accretion and differentiation. Geochimica et Cosmochimica Acta 73, 5189-5201.
Warren, P.H., Ulff-Møller, F., Huber, H., Kallemeyn, G.W., 2006. Siderophile geochemistry of ureilites: A record of early stages of planetesimal core formation. Geochimica et Cosmochimica Acta 70, 2104-2126.
Weiss, B.P., Berdahl, J.S., Elkins-Tanton, L., Stanley, S., Lima, E.A., Carporzen, L., 2008. Magnetism on the angrite parent body and the early differentiation of planetesimals. Science 322, 713-716.
Williams, C.D., Sanborn, M.E., Defouilloy, C., Yin, Q.-Z., Kita, N.T., Ebel, D.S., Yamakawa, A., Yamashita, K., 2020. Chondrules reveal large-scale outward transport of inner Solar System materials in the protoplanetary disk. Proceedings of the National Academy of Sciences, 23426-23435.
Wimpenny, J., Sanborn, M.E., Koefoed, P., Cooke, I.R., Stirling, C., Amelin, Y., Yin, Q.-Z., 2019. Reassessing the origin and chronology of the unique achondrite Asuka 881394: Implications for distribution of 26Al in the early Solar System. Geochimica et Cosmochimica Acta 244, 478-501.
Yamaguchi, A., Clayton, R.N., Mayeda, T.K., Ebihara, M., Oura, Y., Miura, Y.N., Haramura, H., Misawa, K., Kojima, H., Nagao, K., 2002. A new source of basaltic meteorites inferred from Northwest Africa 011. Science 296, 334-336.
Yamashita, K., Maruyama, S., Yamakawa, A., Nakamura, E., 2010. 53Mn-53Cr chronometry of CB chondrite: Evidence for uniform distribution of 53Mn in the early solar system. The Astrophysical Journal 723, 20.
Zhu, K., Liu, J., Moynier, F., Qin, L., Alexander, C.M.O.D., He, Y., 2019a. Chromium isotopic evidence for an early formation of chondrules from the Ornans CO chondrite. The Astrophysical Journal 873, 82.
Zhu, K., Moynier, F., Barrat, J.-A., Wielandt, D., Larsen, K., Bizzarro, M., 2019b. Timing and origin of the angrite parent body inferred from Cr isotopes. The Astrophysical Journal Letters 877, L13.
Zhu, K., Moynier, F., Schiller, M., Alexander, C.M.O.D., Davidson, J., Schrader, D.L., van Kooten, E.M.M.E., Bizzarro, M., 2021a. Chromium isotopic insights into the origin of chondrite parent bodies and the early terrestrial volatile depletion. Geochimica et Cosmochimica Acta 301, 158-186.
Zhu, K., Moynier, F., Schiller, M., Barrat, J.A., Becker, H., Bizzarro, M., 2021b. Tracing the origin and core formation of the enstatite achondrite parent bodies using Cr isotopes. Geochimica et Cosmochimica Acta 308, 256-272.
Zhu, K., Moynier, F., Schiller, M., Bizzarro, M., 2020a. Dating and tracing the origin of enstatite chondrite chondrules with Cr isotopes. The Astrophysical Journal Letters 894, L26.
Zhu, K., Moynier, F., Schiller, M., Wielandt, D., Larsen, K., van Kooten, E., Bizzarro, M., 2020b. Chromium isotopic constraints on the origin the ureilite parent body. The Astrophysical Journal 888, 126.

674

Supplementary Materials:

Radiogenic chromium isotope evidence for the earliest planetary volcanism and crust formation in the solar system

Ke Zhu (朱柯)[1,4]*, Harry Becker[1], Shi-Jie Li[2], Yan Fan[2,3], Xiao-Ning Liu[4] and Tim Elliott[4]

[1] Freie Universität Berlin, Institut für Geologische Wissenschaften, Malteserstr. 74-100, Berlin 12249, Germany

[2] Center for Lunar and Planetary Sciences, Institute of Geochemistry, Chinese Academy of Sciences, Guiyang 550081 China

[3] Department of Geology, Northwest University, Xi'an 710069, China

[4] Bristol Isotope Group, School of Earth Sciences, University of Bristol, Wills Memorial Building, Queen's Road, Bristol BS8 1RJ, United Kingdom

*corresponding author: ke.zhu@bristol.ac.uk

S1. Sample preparation

About 200 mg of a chip of Erg Chech 002 was cut and crushed to grain sizes less than 120 mesh (125 µm). Another ~200 mg chip was crushed and ground into powder for whole rock sample analysis. Minerals were picked under a binocular microscope with a fine needle. After mineral separation, we weighed the samples into cleaned beakers. The sample dissolution procedure involved heating in concentrated HF and HNO_3 (2:1) at 140 °C for two days on a hotplate. After drying down, 2 ml concentrated HNO_3 were added into the beaker and the solution was dried down again to dissolve fluorides. Subsequently, 2 ml concentrated HNO_3 was added to the dried sample and the beakers were placed into Parr pressure vessels within steel jackets for further dissolution at 180 °C over another two days. This way we ensured the complete digestion of fluorides, and refractory phases such as chromites or spinels. Note that, SP2 is a leaching residue from XPX after the first HF+HNO_3 step (on hot plate). Hence, SP2 was digested in concentrated HNO_3 in pressure vessels only. After complete digestion, a ~5% aliquot was used for determination of $^{55}Mn/^{52}Cr$ ratios and major element contents, ~50% of the digestion was used for purification of Cr by a three-step column chemistry described in Zhu et al. (2021c) for mass-independent Cr isotopic analyses. The remaining 45% portion is planned for mass-dependent Cr isotope analysis.

S2. Methods

S2.1 Petrological observation

Petrological observation was conducted using a FEI-Scios field emission scanning electron microscope (FE-SEM) equipped with an EDAX energy-dispersive detection system (EDS) at the Institute of Geochemistry, Chinese Academy of Sciences (IGCAS). The accelerating voltage is 15-30 kV, and the electron beam current is 0.8-1.6 nA. Note that the sample portion in the petrological study is different from the samples used for isotope analysis.

S2.2 Mineral compositions

Mineral compositions were determined by the JXA 8230 electron microprobe analysis (EMPA) at State Key Laboratory of Ore Deposit Geochemistry, Institute of Geochemistry, CAS. The following natural standards were used: olivine for Fe, Si, Mg and Ni, pyrope for Mn, Ti, Cr, Ca and Al, albite for Na, orthoclase for K, and apatite for P in pyroxene analyses; $FeCr_2O_4$ for Fe, Cr, Mg and Al, pyrope for Mn, Ti, Si, Ca, olivine for Ni, albite for Na, apatite for P in spinel and ilmenite analyses;. pyrope for Fe, Mn, Cr and Mg, benitoite for Ba, albite for Na, plagioclase for Si, Al and Ca, orthoclase for K in plagioclase and silica analyses. The measurements were carried out at an accelerating voltage of 25 kV with an electron beam current of 10 nA. The beam diameter varies from 1 to 10 μm. Data reduction was conducted with a standard ZAF-correction procedure.

S2.3 Isotope and elemental analysis

The purification of Cr followed the cation column chemistry as originally described in Trinquier et al. (2008) and modified in Zhu et al. (2019b). Low-yield (e.g., < 70%) Cr purification may produce large equilibrium mass-dependent Cr isotope fractionation from column chemistry which cannot be well corrected using the exponential mass fractionation law (Qin et al., 2010; Trinquier et al., 2008). Thus, similar to the method used in Moynier et al. (2011), we used 3 (1 + 1 + 1) mL of 6M HCl for washing the column and we collected the matrix material, containing residual Cr on the resin in the first cation column (containing 1 ml resin) and re-passed the collected Cr on this first column to ensure yields ranging from 88% to 99% (average of 93%). In the second column, we used four times 0.4 ml 6N HCl (total 1.6 ml) to collect Cr, instead of a total 3 ml 6N HCl (Trinquier et al., 2008). In this way, the organics in purified Cr from the resin are deceased, which can be detrimental for Cr thermal ionization. The final purified Cr was dissolved in ~0.2 ml 30% H_2O_2 and heated on a hotplate at 50 – 60 °C for an hour in order to minimize contamination of the Cr fraction with organics from the resin (Zhu et al., 2021a). The blank of the full chemical purification is between 0.5 and 2 ng that is negligible for the samples with > 1μg of Cr. Mass-independent Cr isotope analysis was performed via the total evaporation method on the Triton TIMS housed at Freie Universität Berlin based on methods described in the literature (Van Kooten et al., 2016; Zhu et al., 2019a; Zhu et al., 2021c; Zhu et al., 2020). Details of TIMS sample loading methods can be found in Zhu et al. (2021a).

NIST 3112a was used as the isotope standard, which has the same mass-independent Cr isotope composition as NIST SRM 979 (Zhu et al., 2021b), used in some other studies. Sample solutions with concentrations of ~15 ppm were prepared, 1µl (containing 15 ng of Cr) of these solutions were loaded on to degassed filaments. Each sample was measured to exhaustion (until all the Cr on the filaments were evaporated) with a pilot ^{52}Cr signal of 10 V for 700 – 1800 cycles and integration time of 1.049s per cycle. The $^{56}Fe/^{52}Cr$ signal ratios were always less than 5×10^{-4}. The $^{53}Cr/^{52}Cr$ and $^{54}Cr/^{52}Cr$ ratios were normalized to a constant $^{50}Cr/^{52}Cr$ ratio of 0.051859 using an exponential law (Lugmair and Shukolyukov, 1998) and are expressed in the epsilon notation:

$$\varepsilon\, ^{x}Cr = \left(\frac{(^{x}Cr/^{52}Cr)_{sample}}{(^{x}Cr/^{52}Cr)_{NIST\ SRM\ 979}} - 1 \right) \times 10000 \quad (1),$$

with x = 53 or 54.

For data quality control, we analysed the Cr isotope composition of the Allende meteorite (CV3 chondrite), DTS-1 (terrestrial dunite), and NIST 3112a processed through the same digestion and chemical separation methods as the samples. Allende-a and Allende-b are from different dissolutions. Allende-b is from 47.2 mg powder ground from ~5g of several bulk meteorite chips, that is assumed to be a representative sample of the bulk chondrite, considering the internal heterogeneity of chondrite samples (Stracke et al., 2012). Four aliquots were taken from the dissolution of Allende-b to test sample reproducibility.

The ε^{53}Cr and ε^{54}Cr data in this study for Allende and terrestrial peridotite DTS-1 are consistent with literature data (Qin et al., 2010; Trinquier et al., 2007; Zhu et al., 2021b). Furthermore, the very small 2SD variation (~0.04 for both ε^{53}Cr and ε^{54}Cr) for multiple analyses of Allende, and the ε^{53}Cr and ε^{54}Cr values close to 0 for NIST 3112a processed through all the column chemistry, strongly support the high quality of the data.

The ^{55}Mn/^{52}Cr ratios were measured on a *Neptune* multiple-collector inductively-coupled-plasma mass-spectrometer (MC-ICP-MS) housed at the University of Bristol, following the method described in Zhu et al. (2021b). The signals of ^{52}Cr, ^{53}Cr and ^{55}Mn were measured on an unpurified aliquot of sample dissolution. The interference of the ^{40}Ar^{12}C peak on ^{52}Cr was mass resolved, and the measured ^{53}Cr/^{52}Cr ratio was monitored and stable at ~0.117. We determined instrument bias using measurements of four gravimetrically prepared solutions of pure standards with ^{55}Mn/^{52}Cr ratios of approximately 0.1, 1, 2 and 10. There was no systematic difference in instrumental bias determined across this range of ^{55}Mn/^{52}Cr and the average value of instrumental bias has an uncertainty in weighing and measurement errors of 1% (2SD). We further measured the ^{55}Mn/^{52}Cr ratios of BIR-1, BHVO-2 and DTS-2b to provide data and standards with more complex matrices which gave values of 3.133, 5.597 and 0.049 respectively. However, lack of literature ^{55}Mn/^{52}Cr data for the three standards make them difficult to be tested. We also test the repeatability of the calibration factor between different Mn/Cr mixes, which is 0.97%, so we quote 1% for the uncertainty of

$^{55}Mn/^{52}Cr$ ratios. All these international rock standards were dissolved in bombs to ensure spinel/chromite dissolution. The elemental contents were measured on *Element XR* ICP-MS housed at University of Bristol, and the uncertainty of elemental content data is estimated as 10%. The elemental content data for bulk EC 002 are consistent with the data in Barrat et al. (2021).

Table S1 Chemical composition of xenocrysts (pyroxenes) from core to rim.

Name	FeO	NiO	MnO	TiO_2	Cr_2O_3	SiO_2	MgO	Mg#	Al_2O_3	CaO	P_2O_5	Total
I Line 001	10.24	0.00	0.47	0.07	0.46	57.01	30.38	0.84	0.21	1.01	0.00	99.86
I Line 002	9.07	0.01	0.48	0.03	0.60	57.34	31.29	0.86	0.23	0.93	0.00	99.99
I Line 003	9.30	0.00	0.43	0.04	0.60	57.11	30.90	0.86	0.20	0.92	0.00	99.52
I Line 004	9.48	0.01	0.46	0.04	0.60	57.01	31.26	0.85	0.19	0.93	0.00	99.98
I Line 005	9.44	0.00	0.43	0.00	0.61	57.44	31.38	0.86	0.20	0.96	0.00	100.46
I Line 006	9.56	0.01	0.45	0.02	0.63	57.56	31.38	0.85	0.17	0.96	0.02	100.76
I Line 007	9.32	0.00	0.46	0.02	0.65	57.43	31.01	0.86	0.19	0.96	0.00	100.03
I Line 008	9.40	0.00	0.45	0.04	0.60	57.35	30.78	0.85	0.20	0.93	0.02	99.77
I Line 009	9.44	0.00	0.51	0.04	0.60	57.52	30.96	0.85	0.18	1.00	0.00	100.25
I Line 010	9.42	0.00	0.41	0.06	0.59	57.79	31.29	0.85	0.20	0.96	0.00	100.72
I Line 011	9.64	0.00	0.46	0.07	0.59	57.72	31.27	0.85	0.19	1.00	0.00	100.93
I Line 012	9.67	0.00	0.45	0.07	0.60	57.48	30.75	0.85	0.22	1.00	0.01	100.25
I Line 013	9.59	0.01	0.48	0.01	0.57	57.65	30.61	0.85	0.18	0.96	0.00	100.05
I Line 014	9.63	0.00	0.46	0.02	0.59	57.18	30.83	0.85	0.22	0.93	0.01	99.86
I Line 015	9.64	0.00	0.49	0.05	0.51	57.47	30.80	0.85	0.24	0.92	0.00	100.12
I Line 016	9.42	0.00	0.47	0.01	0.53	57.50	30.86	0.85	0.21	0.91	0.00	99.90
I Line 017	10.17	0.00	0.44	0.07	0.60	57.89	30.64	0.84	0.19	0.81	0.01	100.82
I Line 018-rim	18.93	0.00	0.66	0.08	0.34	54.22	23.61	0.69	0.16	0.67	0.00	98.67
I Line 019-rim	23.31	0.00	0.81	0.13	0.28	53.19	20.85	0.61	0.14	0.89	0.00	99.59
I Line 020-rim	21.91	0.00	1.03	0.21	0.33	53.65	19.10	0.61	0.15	4.05	0.00	100.42
II Line 001	12.01	0.01	0.64	0.01	0.45	56.46	27.50	0.80	0.22	1.75	0.00	99.04
II Line 002	11.75	0.00	0.56	0.02	0.57	55.96	27.90	0.81	0.25	1.84	0.04	98.90
II Line 003	11.81	0.01	0.58	0.01	0.67	56.53	28.24	0.81	0.21	1.92	0.00	99.97
II Line 004	11.64	0.00	0.56	0.04	0.75	56.71	28.04	0.81	0.26	1.90	0.00	99.89
II Line 005	11.65	0.00	0.59	0.05	0.72	56.16	27.88	0.81	0.27	1.86	0.02	99.20
II Line 006	11.33	0.00	0.58	0.03	0.65	56.82	28.35	0.82	0.30	1.85	0.04	99.95
II Line 007	11.27	0.01	0.58	0.07	0.58	56.69	27.99	0.82	0.27	1.74	0.00	99.21
II Line 008	11.31	0.00	0.58	0.08	0.55	55.94	28.98	0.82	0.25	1.82	0.00	99.50
II Line 009	11.29	0.01	0.60	0.05	0.61	56.09	28.71	0.82	0.23	1.73	0.00	99.31
II Line 010	11.28	0.00	0.59	0.00	0.79	57.04	28.17	0.82	0.22	1.85	0.02	99.94
II Line 011	11.19	0.01	0.63	0.04	0.81	56.30	28.15	0.82	0.27	1.86	0.00	99.25
II Line 012	11.36	0.00	0.60	0.08	0.82	55.90	28.39	0.82	0.31	1.84	0.04	99.34
II Line 013	11.39	0.00	0.59	0.05	0.85	55.76	27.87	0.81	0.29	1.78	0.00	98.57
II Line 014	11.20	0.00	0.57	0.06	0.87	57.40	27.91	0.82	0.28	1.91	0.00	100.19
II Line 015	11.38	0.02	0.59	0.04	0.85	56.63	28.09	0.81	0.27	1.95	0.00	99.81
II Line 016	11.39	0.00	0.64	0.08	0.82	56.46	28.10	0.81	0.29	1.86	0.03	99.65
II Line 017	11.50	0.00	0.59	0.06	0.74	56.39	28.49	0.81	0.28	1.97	0.00	100.02
II Line 018	11.68	0.00	0.56	0.06	0.70	56.39	28.29	0.81	0.26	1.93	0.02	99.87
II Line 019	11.99	0.00	0.56	0.05	0.67	55.94	28.07	0.81	0.26	1.84	0.00	99.38
II Line 020	12.41	0.00	0.60	0.06	0.62	55.69	27.87	0.80	0.29	1.87	0.00	99.40

II Line 021-rim	13.10	0.01	0.60	0.05	0.58	56.28	27.23	0.79	0.27	1.88	0.00	100.00
II Line 022-rim	21.38	0.00	0.88	0.08	0.31	54.25	21.22	0.64	0.27	1.39	0.00	99.80
II Line 023-rim	14.18	0.00	0.66	0.33	0.93	52.88	13.96	0.64	0.66	15.08	0.00	98.69
II Line 024-rim	14.82	0.00	0.69	0.60	0.85	53.05	12.95	0.61	0.59	15.24	0.00	98.80
III Line 001	11.36	0.00	0.70	0.02	0.62	56.39	25.88	0.80	0.26	4.67	0.00	99.92
III Line 002	10.53	0.00	0.59	0.02	0.56	56.28	26.00	0.81	0.30	5.76	0.00	100.05
III Line 003	11.38	0.00	0.61	0.05	0.40	55.66	27.85	0.81	0.28	2.48	0.00	98.72
III Line 004	12.47	0.01	0.68	0.03	0.51	56.04	27.42	0.80	0.28	2.25	0.00	99.68
III Line 005	11.12	0.00	0.66	0.07	0.67	55.21	25.70	0.80	0.28	4.82	0.03	98.55
III Line 006	11.43	0.01	0.66	0.08	0.57	55.26	25.67	0.80	0.22	4.55	0.02	98.44
III Line 007	11.65	0.00	0.65	0.07	0.57	56.38	25.89	0.80	0.28	4.37	0.00	99.86
III Line 008	11.65	0.00	0.67	0.05	0.66	56.82	25.14	0.79	0.33	4.31	0.00	99.63
III Line 009	10.22	0.00	0.59	0.06	0.84	55.73	24.08	0.81	0.40	6.85	0.03	98.78
III Line 010	12.91	0.00	0.68	0.01	0.51	56.00	26.06	0.78	0.19	2.97	0.00	99.31
III Line 011	11.73	0.00	0.67	0.05	0.60	55.05	25.22	0.79	0.28	4.85	0.03	98.49
III Line 012	10.11	0.00	0.56	0.03	0.75	56.06	22.62	0.80	0.34	8.81	0.01	99.28
III Line 013	10.97	0.00	0.54	0.05	0.70	56.10	23.54	0.79	0.41	7.43	0.02	99.74
III Line 014-rim	15.48	0.00	0.74	0.01	0.48	54.75	23.54	0.73	0.21	3.87	0.00	99.07
III Line 015-rim	22.48	0.00	0.96	0.11	0.51	52.90	16.92	0.57	0.35	4.97	0.00	99.18
III Line 016-rim	15.18	0.00	0.68	0.45	0.79	53.16	12.49	0.59	0.45	15.87	0.05	99.13
III Line 017-rim	15.36	0.00	0.71	0.65	0.79	52.65	12.21	0.59	0.39	15.91	0.01	98.69
III Line 018-rim	15.15	0.00	0.69	0.85	0.79	52.76	12.02	0.58	0.33	16.51	0.02	99.12
III Line 019-rim	16.21	0.00	0.69	0.83	0.83	53.06	11.99	0.57	0.53	15.72	0.00	99.86
III Line 020-rim	15.49	0.00	0.66	1.07	0.80	52.10	11.50	0.57	0.39	16.44	0.03	98.48

Note: The location of the three lines can be found in Figure S1.

Table S2 Chemical composition of pyroxenes in matrix.

Name	FeO	NiO	MnO	TiO_2	Cr_2O_3	Na_2O	SiO_2	MgO	Mg#	Al_2O_3	K_2O	CaO	P_2O_5	Total
low-Ca pyroxene														
Opx-M1	32.77	0.00	1.26	0.41	0.19	0.03	49.98	14.05	0.43	0.12	0.00	2.09	0.00	100.89
Opx-M2	32.23	0.00	1.22	0.41	0.16	0.09	49.72	14.08	0.44	0.13	0.00	1.89	0.00	99.91
Opx-M3	32.03	0.00	1.26	0.42	0.19	0.06	49.72	14.12	0.44	0.10	0.00	2.26	0.00	100.15
Opx-M4	31.88	0.00	1.24	0.50	0.20	0.07	49.88	14.47	0.45	0.13	0.00	2.31	0.04	100.71
Opx-M5	32.34	0.00	1.25	0.47	0.27	0.02	49.66	14.64	0.45	0.11	0.00	1.89	0.00	100.64
Opx-M6	32.07	0.00	1.24	0.17	0.27	0.08	50.66	14.34	0.44	0.16	0.00	2.14	0.00	101.13
Opx-M7	31.92	0.00	1.22	0.21	0.26	0.07	50.56	14.67	0.45	0.21	0.00	2.26	0.02	101.41
Opx-M8	32.45	0.00	1.28	0.43	0.21	0.02	49.70	13.94	0.43	0.06	0.00	2.15	0.00	100.23
Opx-M9	32.21	0.00	1.22	0.45	0.15	0.12	50.14	14.26	0.44	0.12	0.00	2.00	0.02	100.70
Opx-M10	32.37	0.00	1.23	0.49	0.18	0.08	49.63	14.03	0.43	0.10	0.00	1.97	0.02	100.10
Opx-M11	32.21	0.00	1.26	0.41	0.21	0.09	50.00	14.04	0.44	0.19	0.00	2.55	0.00	100.94
Opx-M12	32.96	0.00	1.32	0.50	0.16	0.08	49.93	14.15	0.43	0.09	0.00	1.97	0.01	101.16
Opx-M13	32.30	0.00	1.25	0.47	0.16	0.11	50.81	14.29	0.44	0.09	0.00	2.21	0.00	101.69
Opx-M14	32.32	0.00	1.26	0.43	0.18	0.13	50.03	14.14	0.44	0.18	0.00	2.01	0.02	100.70
Opx-M15	31.58	0.00	1.22	0.46	0.20	0.05	50.02	14.13	0.44	0.12	0.00	2.39	0.05	100.22
high-Ca pyroxene														
Cpx-M1	16.10	0.00	0.63	0.96	0.71	0.48	51.38	11.24	0.55	0.43	0.00	17.74	0.00	99.67
Cpx-M2	16.49	0.00	0.67	0.83	0.89	0.62	50.87	11.46	0.55	0.74	0.00	17.08	0.02	99.68
Cpx-M3	17.30	0.00	0.73	1.11	0.72	0.52	51.21	11.50	0.54	0.39	0.00	16.80	0.02	100.29
Cpx-M4	17.96	0.01	0.73	0.88	0.76	0.54	51.85	11.52	0.53	0.57	0.00	15.92	0.02	100.74
Cpx-M5	16.61	0.00	0.65	0.90	0.76	0.63	51.92	11.47	0.55	0.47	0.00	17.15	0.00	100.56
Cpx-M6	16.73	0.00	0.69	0.93	0.77	0.52	51.41	11.40	0.55	0.45	0.01	17.01	0.03	99.93
Cpx-M7	16.48	0.00	0.66	0.96	0.75	0.49	51.94	11.45	0.55	0.42	0.01	17.33	0.01	100.47
Cpx-M7-repeat	16.26	0.00	0.65	0.93	0.71	0.57	51.27	11.65	0.56	0.57	0.01	17.26	0.02	99.90
Cpx-M8	17.49	0.00	0.71	0.83	0.65	0.47	49.69	11.75	0.54	0.33	0.01	16.13	0.02	98.06
Cpx-M8-repeat	17.20	0.00	0.69	0.39	0.86	0.45	50.41	11.59	0.54	0.67	0.00	16.57	0.05	98.87
Cpx-M9	16.06	0.00	0.61	0.81	0.71	0.46	50.79	11.87	0.57	0.30	0.00	18.21	0.01	99.82
Cpx-M9-repeat	16.14	0.00	0.67	1.10	0.74	0.56	50.17	11.79	0.56	0.52	0.01	17.26	0.00	98.95
Cpx-M10	17.15	0.00	0.71	1.03	0.72	0.52	50.03	11.28	0.54	0.39	0.01	16.91	0.05	98.77
Cpx-M11	16.38	0.00	0.68	0.83	0.88	0.47	49.65	11.32	0.55	0.76	0.00	17.07	0.00	98.03
Cpx-M12	16.57	0.00	0.70	0.59	0.95	0.67	52.44	12.04	0.56	0.89	0.00	17.11	0.03	101.98
Cpx-M13	16.20	0.00	0.66	0.92	0.69	0.37	51.20	11.66	0.56	0.37	0.00	17.81	0.05	99.94
Cpx-M14	16.36	0.00	0.68	0.96	0.76	0.44	50.31	11.52	0.56	0.42	0.00	17.15	0.04	98.63
Cpx-M15	16.59	0.00	0.68	0.78	0.80	0.48	50.04	11.38	0.55	0.53	0.00	17.22	0.01	98.50

Table S3 Chemical composition of plagioclase in matrix

Comment	FeO	MnO	BaO	Cr_2O_3	Na_2O	SiO_2	MgO	Al_2O_3	K_2O	CaO	Total
Normal											
pl-1	0.07	0.00	0.00	0.00	9.75	65.76	0.00	20.19	0.65	1.89	98.30
pl-2	0.10	0.00	0.00	0.01	9.90	65.91	0.00	19.93	0.99	1.74	98.57
pl-3	0.05	0.02	0.00	0.01	9.47	64.83	0.00	20.98	0.84	2.40	98.59
pl-4	0.07	0.00	0.00	0.02	9.14	63.30	0.00	21.86	0.52	3.74	98.65
pl-5	0.04	0.00	0.01	0.02	9.70	65.30	0.00	20.48	0.90	2.12	98.57
K-rich											
Kfs-1	1.30	0.00	0.00	0.00	1.30	63.54	0.00	18.83	13.96	0.79	99.73
Kfs-2	0.95	0.01	0.00	0.00	1.97	63.93	0.00	18.44	12.41	0.81	98.52
Kfs-3	0.88	0.01	0.06	0.01	2.52	65.05	0.00	18.96	11.22	0.83	99.54
Kfs-4	0.47	0.00	0.07	0.02	2.10	64.14	0.00	18.61	12.08	0.84	98.32
Kfs-5	0.57	0.00	0.02	0.01	1.74	64.37	0.00	18.47	12.70	0.89	98.77

Table S4 Chemical composition of silica in matrix and xenocrysts

Name	FeO	MnO	BaO	Cr2O3	Na2O	SiO2	MgO	Al2O3	K2O	CaO	Total
Matrix											
SiO2-M1	0.18	0.01	0.02	0.00	1.30	94.50	0.00	2.56	0.01	0.13	98.71
SiO2-M2	0.04	0.01	0.00	0.00	1.44	95.62	0.00	2.65	0.02	0.14	99.92
SiO2-M3	0.07	0.00	0.00	0.02	1.27	94.79	0.01	2.50	0.01	0.14	98.80
SiO2-M4	0.11	0.00	0.00	0.00	1.24	95.63	0.00	2.57	0.00	0.13	99.69
SiO2-M5	0.10	0.00	0.00	0.00	1.02	97.80	0.03	2.34	0.01	0.10	101.40
SiO2-M6	0.02	0.00	0.00	0.01	1.14	94.62	0.00	2.22	0.01	0.08	98.10
SiO2-M7	0.14	0.01	0.01	0.00	1.23	96.59	0.00	2.32	0.01	0.10	100.41
SiO2-M8	0.05	0.00	0.00	0.00	1.21	95.76	0.00	2.26	0.00	0.09	99.37
Xenocrysts											
SiO2-X1	0.37	0.01	0.04	0.01	3.03	72.82	0.05	15.42	8.22	0.27	100.23
SiO2-X2	0.46	0.01	0.00	0.29	2.56	71.73	0.01	14.86	8.21	0.21	98.34

Table S5 Chemical composition of ilmenite and spinel in matrix and xenocrysts

Name	FeO	MnO	NiO	TiO_2	Cr_2O_3	Na_2O	SiO_2	MgO	Mg#	Al_2O_3	CaO	P_2O_5	Total
Ilmenite in matrix													
Ilm-M1	42.84	1.02	0.00	52.59	0.86	0.08	0.13	1.41	0.06	0.06	0.00	0.01	98.99
Ilm-M2	43.40	1.04	0.00	53.15	0.34	0.00	0.12	1.63	0.06	0.04	0.01	0.01	99.73
Ilm-M3	43.33	1.03	0.00	52.42	0.70	0.05	0.15	1.35	0.05	0.04	0.00	0.00	99.07
Spinel in matrix													
Sp-M1	39.66	0.83	0.00	13.03	41.98	0.00	0.13	1.00	0.04	2.72	0.01	0.00	99.36
Sp-M2	39.41	0.73	0.00	11.99	43.47	0.03	0.14	1.04	0.04	3.18	0.05	0.01	100.06
Sp-M3	45.25	0.89	0.01	20.69	31.51	0.07	0.11	1.05	0.04	1.49	0.00	0.00	101.08
Sp-M4	40.44	0.85	0.01	13.71	41.07	0.01	0.13	1.00	0.04	2.46	0.00	0.00	99.68
Sp-M5	45.62	0.86	0.00	20.56	30.62	0.00	0.22	1.04	0.04	1.30	0.00	0.02	100.24
Sp-M6	42.44	0.81	0.00	16.54	35.76	0.00	0.20	1.17	0.05	1.62	0.03	0.00	98.57
Sp-M7	42.38	0.79	0.00	16.32	38.65	0.01	0.16	1.02	0.04	1.94	0.00	0.00	101.25
Sp-M8	42.64	0.76	0.00	16.48	38.43	0.01	0.08	0.97	0.04	1.97	0.00	0.00	101.35
Sp-M9	45.20	0.85	0.02	18.74	32.58	0.02	0.12	1.05	0.04	1.37	0.30	0.01	100.26
Sp-M10	41.74	0.82	0.00	16.09	36.68	0.01	0.27	1.18	0.05	1.61	0.32	0.00	98.72
Spinel in xenocrysts													
Sp-X1	29.13	0.72	0.00	1.20	51.34	0.00	0.09	2.63	0.14	11.66	0.00	0.00	96.77
Sp-X2	24.18	0.83	0.00	0.38	55.06	0.00	0.24	5.25	0.28	8.57	0.04	0.00	94.55

Table S6 Age comparison for achondrites between U-Pb, Mn-Cr and Al-Mg chronometry

Sample	CC/NC	Type	U-Pb	Mn-Cr	Al-Mg (D')	Al-Mg (CAI)	Initial μ^{26}Mg*	Bulk ε^{54}Cr	References
Erg Chech 002	NC	Brachinite-like		4566.5 ± 0.6	4566.6 ± 0.01	4565.4 ± 0.01	-9 ± 5	-0.35 ± 0.06	This study; [a]
Asuka 881394	NC	Achondrite	4564.95 ± 0.53	4564.3 ± 0.4	4564.83 ± 0.21	4563.69 ± 0.36	70 ± 52	-0.37 ± 0.10	[b, c]
Sahara 99555	NC	Angrite	4563.93 ± 0.28	4562.7 ± 0.8	4563.5 ± 0.1	4562.3 ± 0.1	5 ± 3	-0.43 ± 0.13	[d, e, f, g]
NWA 6704	CC	CR-like achondrite	4562.6 ± 0.3	4562.17 ± 0.76	4563.12 ± 0.1	4561.9 ± 0.1	-4 ± 5	1.56 ± 0.10	[h, i]
NWA 2976	CC	Achondrite	4562.86 ± 0.59		4563.4 ± 0.1	4562.2 ± 0.1	-5 ± 13	1.43 ± 0.07	[h, j]

References: [a] (Fang et al., 2022), [b] (Wadhwa et al., 2009), [c] (Wimpenny et al., 2019) , [d] (Schiller et al., 2010), [e] (Connelly et al., 2008), [f] (Amelin, 2008), [g] (Tissot et al., 2017), [h] (Sanborn et al., 2019), [i] (Amelin et al., 2019), [j] (Bouvier et al., 2011).

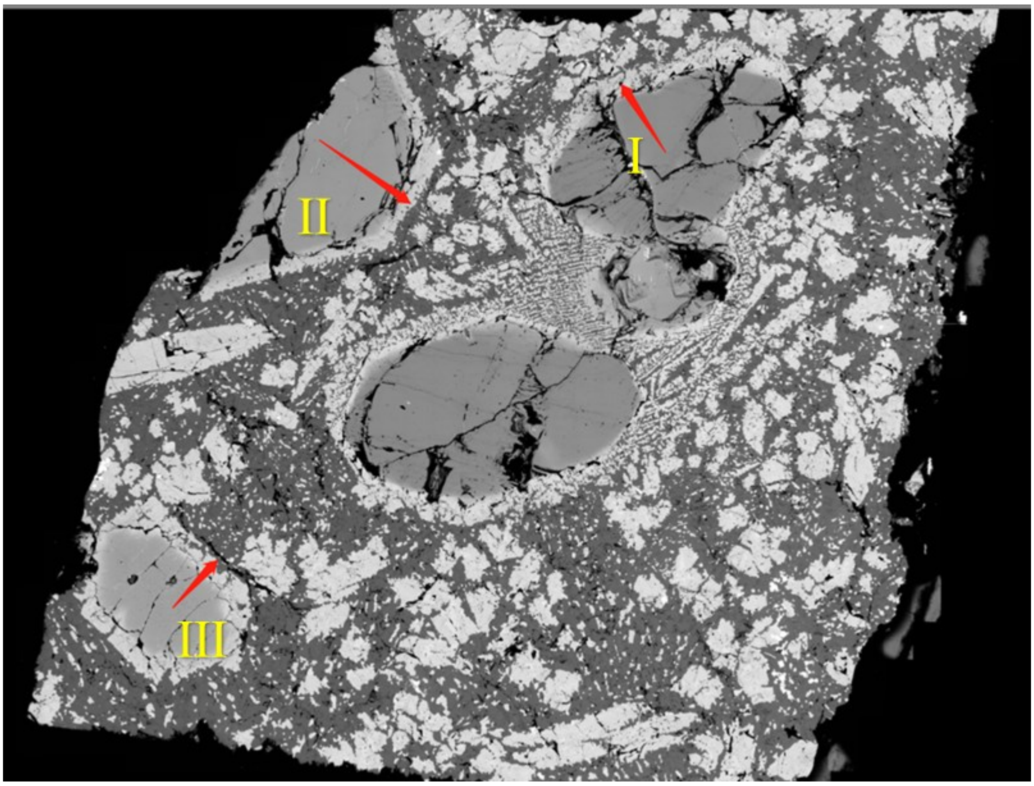

Figure S1 Electronic microprobe analysis for lines on xenocrysts. The red arrows indicate the line measurements. The data can be found in Table S1

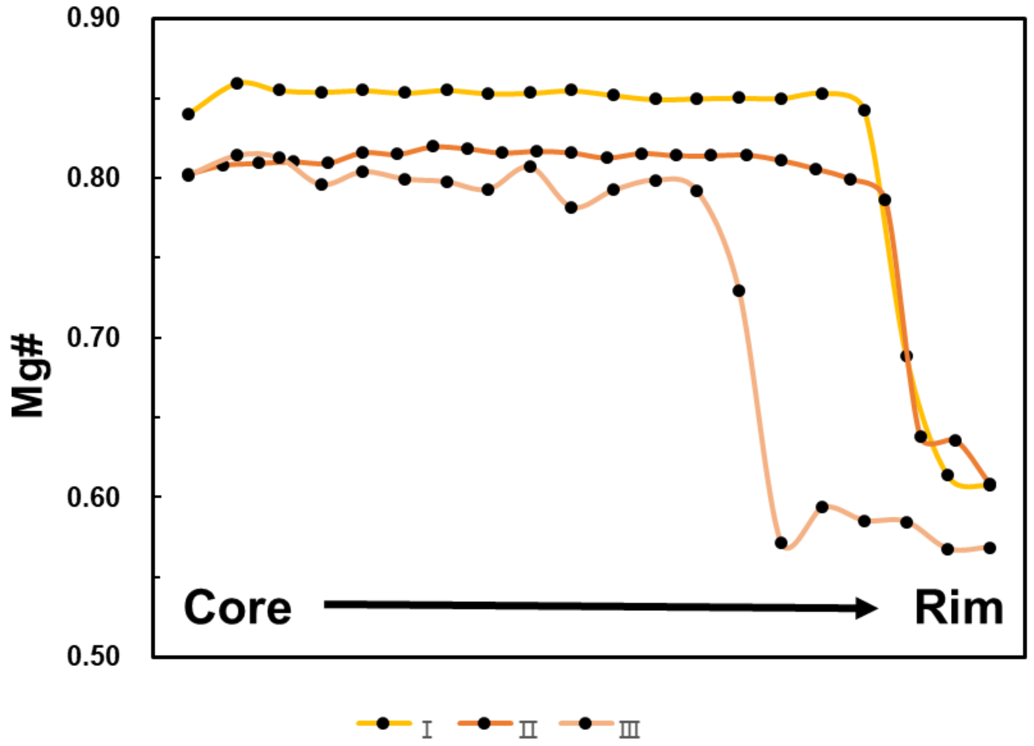

Figure S2 Mg# variation of EC 002 xenocrysts from core to rim. Lines I II III can be found in Figure S1.

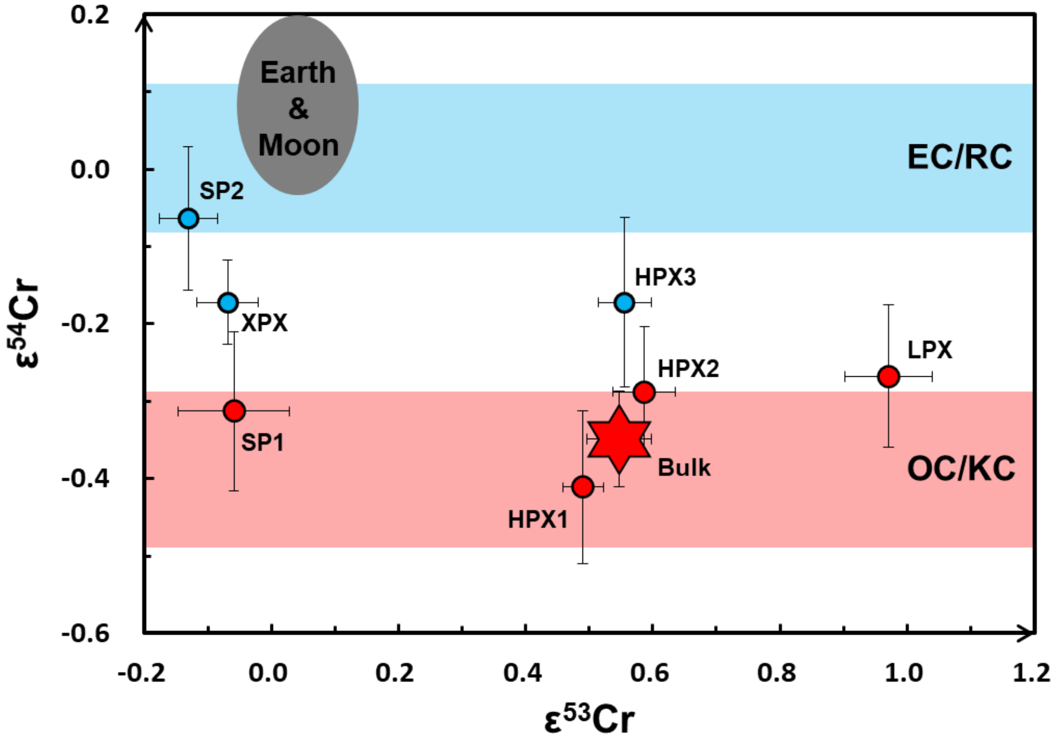

Figure S3 A ε^{53}Cr-ε^{54}Cr plot for Erg Chech (EC) 002 and its components. Names of each point are from Table 1. The red points are similar to the bulk rock (star) in ε^{54}Cr, while the blue points possess higher ε^{54}Cr values. Reference values for EC (enstatite chondrites), RC (Rumuruti chondrites), OC (ordinary chondrites), KC (Kakangari chondrites) and the Earth-Moon system are from Zhu et al. (2021b) and Zhu et al. (2022).

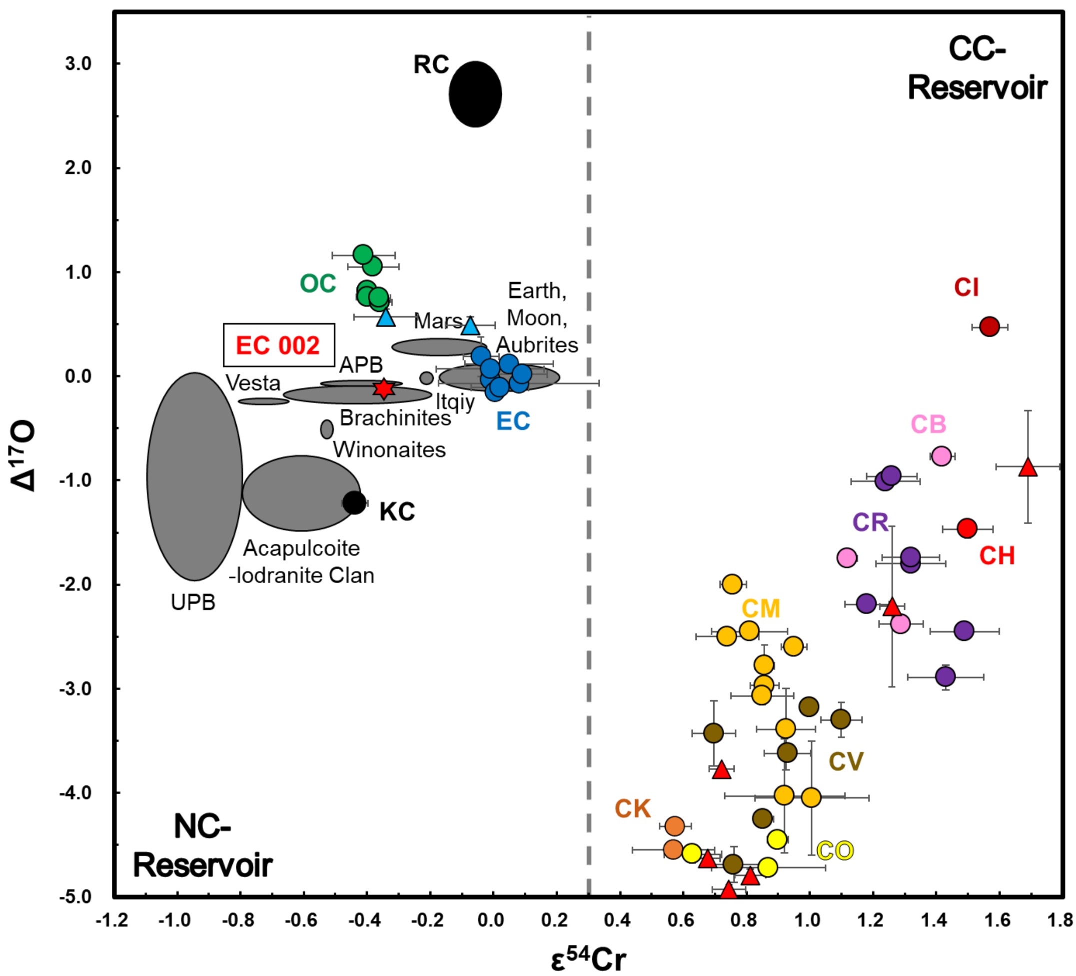

Figure S4 Plot of $\Delta^{17}O$-$\varepsilon^{54}Cr$ for Erg Chech (EC) 002 (Red Star) and other Solar System materials. The diagram is divided into carbonaceous chondrite-like (CC) and non-carbonaceous (NC) fields, seperated by a dashed line. The colorful circles and triangles represent grouped and ungrouped chondrites respectively (labelled with standard abbreviations), while the grey shades represent compositional fields of differentiated planets/asteroids (data compilation from Zhu et al. (2021b) and Zhu et al. (2022). The $\Delta^{17}O$-$\varepsilon^{54}Cr$ data for EC 002 (red star) overlaps the brachinites.

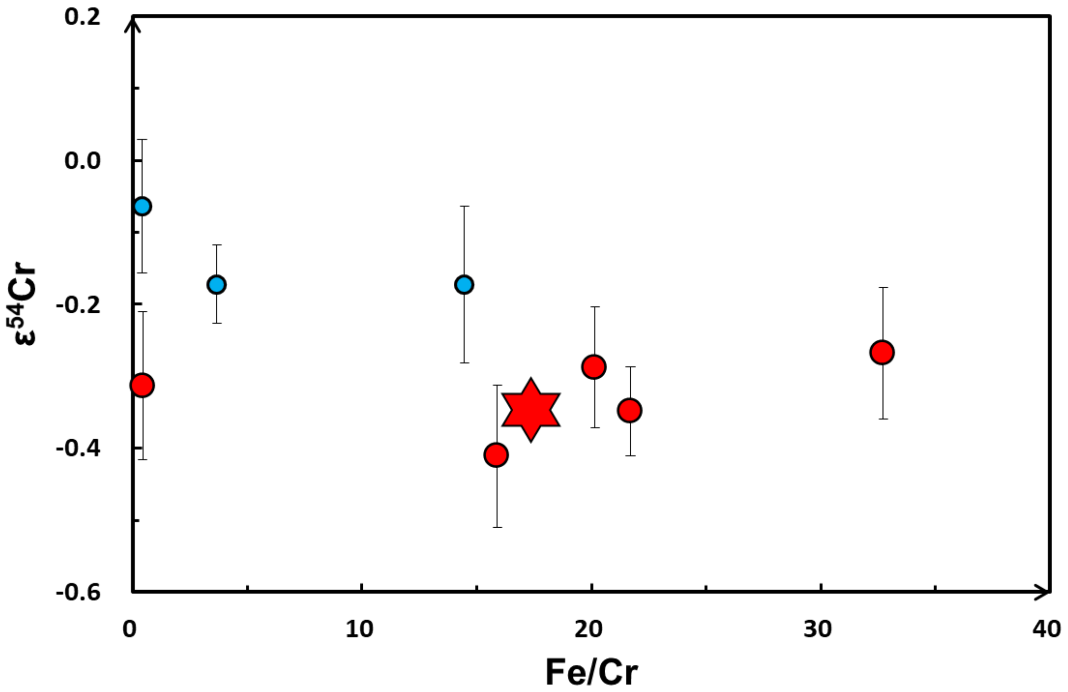

Figure S5 Lack of correlation between Fe/Cr ratios (atom) and $\varepsilon^{54}Cr$ values indicates cosmogenic effects did not affect the Cr isotope compositions in EC 002. Red and blue points are normal and xenocrysts-related components

References:

Amelin, Y., 2008. The U–Pb systematics of angrite Sahara 99555. Geochimica et Cosmochimica Acta 72, 4874-4885.

Amelin, Y., Koefoed, P., Iizuka, T., Assis Fernandes, V., Huyskens, M.H., Yin, Q.-Z., Irving, A.J., 2019. U-Pb, Rb-Sr and Ar-Ar systematics of the ungrouped achondrites Northwest Africa 6704 and Northwest Africa 6693. Geochimica et Cosmochimica Acta, 628-642.

Barrat, J.-A., Chaussidon, M., Yamaguchi, A., Beck, P., Villeneuve, J., Byrne, D.J., Broadley, M.W., Marty, B., 2021. A 4,565-My-old andesite from an extinct chondritic protoplanet. Proceedings of the National Academy of Sciences 118, e2026129118.

Bouvier, A., Spivak-Birndorf, L.J., Brennecka, G.A., Wadhwa, M., 2011. New constraints on early Solar System chronology from Al–Mg and U–Pb isotope systematics in the unique basaltic achondrite Northwest Africa 2976. Geochimica et Cosmochimica Acta 75, 5310-5323.

Connelly, J.N., Bizzarro, M., Thrane, K., Baker, J.A., 2008. The Pb–Pb age of Angrite SAH99555 revisited. Geochimica et Cosmochimica Acta 72, 4813-4824.

Fang, L., Frossard, P., Boyet, M., Bouvier, A., Barrat, J.-A., Chaussidon, M., Moynier, F., 2022. Half-life and initial Solar System abundance of 146Sm determined from the oldest andesitic meteorite. Proceedings of the National Academy of Sciences 119, e2120933119.

Lugmair, G., Shukolyukov, A., 1998. Early solar system timescales according to 53 Mn-53 Cr systematics. Geochimica et Cosmochimica Acta 62, 2863-2886.

Moynier, F., Yin, Q.-Z., Schauble, E., 2011. Isotopic evidence of Cr partitioning into Earth's core. Science 331, 1417-1420.

Qin, L., Alexander, C.M.O.D., Carlson, R.W., Horan, M.F., Yokoyama, T., 2010. Contributors to chromium isotope variation of meteorites. Geochimica et Cosmochimica Acta 74, 1122-1145.

Sanborn, M.E., Wimpenny, J., Williams, C.D., Yamakawa, A., Amelin, Y., Irving, A.J., Yin, Q.-Z., 2019. Carbonaceous Achondrites Northwest Africa 6704/6693: Milestones for Early Solar System Chronology and Genealogy. Geochimica et Cosmochimica Acta 245, 577-596.

Schiller, M., Baker, J.A., Bizzarro, M., 2010. 26Al–26Mg dating of asteroidal magmatism in the young Solar System. Geochimica et Cosmochimica Acta 74, 4844-4864.

Stracke, A., Palme, H., Gellissen, M., Münker, C., Kleine, T., Birbaum, K., Günther, D., Bourdon, B., Zipfel, J., 2012. Refractory element fractionation in the Allende meteorite: Implications for solar nebula condensation and the chondritic composition of planetary bodies. Geochimica et Cosmochimica Acta 85, 114-141.

Tissot, F.L.H., Dauphas, N., Grove, T.L., 2017. Distinct 238U/235U ratios and REE patterns in plutonic and volcanic angrites: Geochronologic implications and evidence for U isotope fractionation during magmatic processes. Geochimica et Cosmochimica Acta 213, 593-617.

Trinquier, A., Birck, J.-L., Allègre, C.J., 2007. Widespread 54Cr heterogeneity in the inner solar system. The Astrophysical Journal 655, 1179-1185.

Trinquier, A., Birck, J.-L., Allègre, C.J., 2008. High-precision analysis of chromium isotopes in terrestrial and meteorite samples by thermal ionization mass spectrometry. Journal of Analytical Atomic Spectrometry 23, 1565-1574.

Van Kooten, E.M.M.E., Wielandt, D., Schiller, M., Nagashima, K., Thomen, A., Larsen, K.K., Olsen, M.B., Nordlund, Å., Krot, A.N., Bizzarro, M., 2016. Isotopic evidence for primordial molecular cloud material in metal-rich carbonaceous chondrites. Proceedings of the National Academy of Sciences 113, 2011-2016.

Wadhwa, M., Amelin, Y., Bogdanovski, O., Shukolyukov, A., Lugmair, G.W., Janney, P., 2009. Ancient relative and absolute ages for a basaltic meteorite: Implications for timescales of planetesimal accretion and differentiation. Geochimica et Cosmochimica Acta 73, 5189-5201.

Wimpenny, J., Sanborn, M.E., Koefoed, P., Cooke, I.R., Stirling, C., Amelin, Y., Yin, Q.-Z., 2019. Reassessing the origin and chronology of the unique achondrite Asuka 881394: Implications for distribution of 26Al in the early Solar System. Geochimica et Cosmochimica Acta 244, 478-501.

Zhu, K., Moynier, F., Alexander, C.M.O.D., Davidson, J., Schrader, D.L., Zhu, J.-M., Wu, G.-L., Schiller, M., Bizzarro, M., Becker, H., 2021a. Chromium Stable Isotope Panorama of Chondrites and Implications for Earth Early Accretion. The Astrophysical Journal 923, 94.

Zhu, K., Moynier, F., Barrat, J.-A., Wielandt, D., Larsen, K., Bizzarro, M., 2019a. Timing and origin of the angrite parent body inferred from Cr isotopes. The Astrophysical Journal Letters 877, L13.

Zhu, K., Moynier, F., Schiller, M., Alexander, C.M.O.D., Davidson, J., Schrader, D.L., van Kooten, E.M.M.E., Bizzarro, M., 2021b. Chromium isotopic insights into the origin of chondrite parent bodies and the early terrestrial volatile depletion. Geochimica et Cosmochimica Acta 301, 158-186.

Zhu, K., Moynier, F., Schiller, M., Barrat, J.A., Becker, H., Bizzarro, M., 2021c. Tracing the origin and core formation of the enstatite achondrite parent bodies using Cr isotopes. Geochimica et Cosmochimica Acta 308, 256-272.

Zhu, K., Moynier, F., Schiller, M., Bizzarro, M., 2020. Dating and tracing the origin of enstatite chondrite chondrules with Cr isotopes. The Astrophysical Journal Letters 894, L26.

Zhu, K., Schiller, M., Moynier, F., Alexander, C.M., Davidson, J., Schrader, D.L., Barrat, J.A., Bizzarro, M., 2022. Chondrite Diversity Revealed by Chromium, Calcium, and Magnesium Isotopes. LPI Contributions 2678, 2317.

Zhu, K., Sossi, P.A., Siebert, J., Moynier, F., 2019b. Tracking the volatile and magmatic history of Vesta from chromium stable isotope variations in eucrite and diogenite meteorites. Geochimica et Cosmochimica Acta 266, 598-610.